MATERIALS SCIENCE

Interfering with proton and electron transfer enables antibacterial starvation therapy

Ji Tan[1]†, Haifeng Zhang[1]†, Yisi Liu[1], Zhenhao Hou[1], Donghui Wang[2], Junjie Zhou[1], Yuanming Cao[3], Shi Qian[1], Bowen Zheng[1], JingJun Nie[4], Yuanyuan Cui[5], Yun Du[6], Kai Huang[6], Shengbing Yang[6], Dafu Chen[4]*, Xuanyong Liu[1,3,7]*

Implant-associated infections are urgently addressed; however, existing materials are difficult to kill bacteria without damaging cells. Here, we propose an innovative concept of selective antibacterial starvation therapy based on interfering with proton and electron transfer on the bacterial membrane. As a proof-of-principle demonstration, a special Schottky heterojunction film composed of gold and alkaline magnesium-iron mixed metal oxides (Au/MgFe-MMO) was constructed on the titanium implant. Once bacteria contacted this implant, the Au/MgFe-MMO film continuously captured the proton and electron participated in respiratory chain of bacteria to impede their energy metabolism, leading to the deficit of adenosine 5′-triphosphate. Prolonged exposure to this starvation state inhibited numerous biosynthesis processes and triggered severe oxidative stress in bacteria, ultimately leading to their death due to DNA and membrane damage. In addition, this heterojunction film was comfortable for mammalian cells, without inhibiting mitochondrial function. This proposed starvation antibacterial therapy gives a notable perspective in designing biosafe smart antibacterial biomaterials.

INTRODUCTION

Infections, especially for implant-associated infections (IAIs), have become one of the most severe postoperative complications (*1*). In the presence of foreign implants, even a small quantity of bacteria may form a biofilm on an implant surface to cause infection (*2*, *3*). Biofilms help bacteria escape host defense and antibiotic chemotherapy, and, therefore, a secondary surgical debridement is often required (*4*, *5*). To prevent IAIs, numerous antibacterial functional surfaces have been proposed on the basis of metal-based antibacterial agent leaching (*6*, *7*), physical structure puncturing (*8*–*10*), thermal damage (*11*, *12*), catalytic reactive oxygen species (ROS) generation (*13*, *14*), electrical stimulation (*15*, *16*), etc. However, designing smart surfaces to efficiently kill bacteria without damaging cells remains a challenge.

The energy metabolism based on the proton-coupled electron transfer respiratory chain is necessary to most mammalian cells and bacteria (*17*). Under the action of a series of enzymes in the respiratory chain, the high-energy electrons generated by biochemical metabolic reactions are transferred step by step (*18*). The energy released from this process pumps the protons to generate a transmembrane proton motive force (PMF) (*19*). Driven by this PMF, protons flow into the bacteria via adenosine 5′-triphosphate (ATP) synthase to produce the energy currency ATP, which supplies energy for various biochemical reactions in cells or bacteria (*20*, *21*). The respiration of mammalian cells and bacteria occurs in different places: The former works on the intracellular inner mitochondrial membrane, while the latter is located on the bacterial membrane, which gives a breakthrough to selectively kill bacteria (*22*). On the basis of the above, we came up with a rational hypothesis that a material with proton-electron regulating capacity may selectively interfere with the bacterial membrane respiration metabolism process to kill bacteria but without affecting the operation of the mitochondria within the cell (Fig. 1). To verify the hypothesis and explore related biological mechanisms, a model material that can capture bacterial membrane electron and proton is required.

In a semiconductor field, numerous advanced heterojunctions are designed to manipulate charge transfer (*23*–*25*). Some special Schottky or type II heterojunctions with suitable energy band structures enable the trapping of protons in solution or the directional transport of electrons from bacterial membranes (*26*–*30*). However, the biocompatibility of the above material systems is nonideal. In addition, usually, only one of the proton or electron transfer can be manipulated, and in this case, bacteria are difficult to be completely killed since the reprogramed metabolic processes. Integrating electron capturing or proton depletion with photo/acoustic thermal/dynamic effects can achieve better synergistic antibacterial performance (*31*–*34*), but the corresponding patient compliance is poor, and the high heat or excess ROS generated by these processes may still damage normal cells or tissues (*35*). Reversely, simultaneously interfering with proton and electron transfer may be more promising to achieve excellent antibacterial effects without damaging normal cells. Unfortunately, it remains a challenge to tailor a proton-electron transfer–regulating material by nonantibacterial chemical components, so as to clarify the underlying antibacterial mechanism based on simultaneously interfering with proton and electron transfer.

The mixed metal oxides (MMOs) derived from hydrotalcite, featuring highly customizable compositions and structures, are promising candidates (*36*, *37*). MMOs, usually as alkaline substances, are proton acceptors that capture the proton, and this capacity can also be

[1]State Key Laboratory of Advanced Ceramics, Shanghai Institute of Ceramics, Chinese Academy of Sciences, Shanghai 200050, China. [2]School of Health Science and Biomedical Engineering, Hebei University of Technology, Tianjin 300130, China. [3]State Key Laboratory for Modification of Chemical Fibers and Polymer Materials, College of Biological Science and Medical Engineering, Donghua University, Shanghai 201620, China. [4]Laboratory of Bone Tissue Engineering, Beijing Laboratory of Biomedical Materials, National Center for Orthopaedics, Beijing Research Institute of Traumatology and Orthopaedics, Beijing Jishuitan Hospital, Capital Medical University, Beijing 100035, China. [5]Shimadzu China Co. Ltd., Shanghai 200233, China. [6]Shanghai Key Laboratory of Orthopaedic Implants, Department of Orthopaedic Surgery, Shanghai Ninth People's Hospital, Shanghai Jiao Tong University School of Medicine, Shanghai 200125, China. [7]School of Chemistry and Materials Science, Hangzhou Institute for Advanced Study, University of Chinese Academy of Sciences, Hangzhou 310024, China.
*Corresponding author. Email: xyliu@mail.sic.ac.cn (X.L.); chendafujst@126.com (D.C.)
†These authors contributed equally to this work.

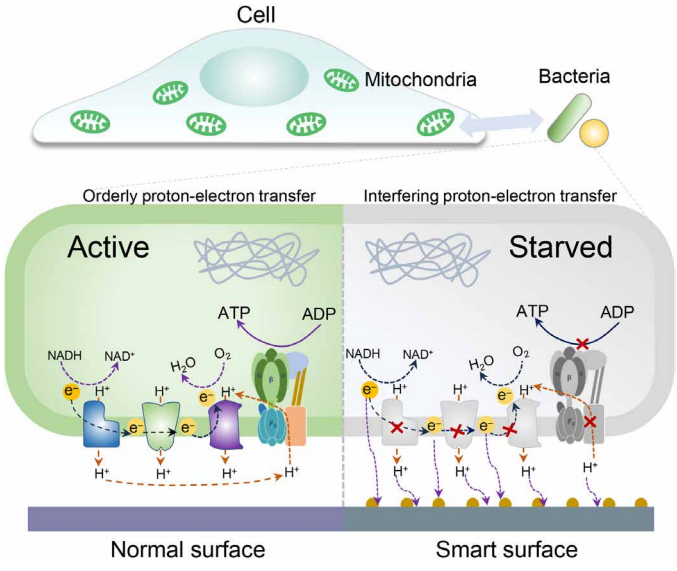

Fig. 1. The illustration of selective antibacterial starvation therapy based on heterojunction functional surface interfering with proton and electron transfer. NAD^+, nicotinamide adenine dinucleotide (oxidized form); NADH, reduced form of NAD^+; ADP, adenosine 5′-diphosphate.

modulated by regulating the types and proportions of divalent/trivalent metal oxides (*38*–*40*). In addition, integrating MMO with a suitable metal or semiconductor can form various heterojunctions to manipulate the electron transfer. Hence, we tailored a Schottky heterojunction array film composed of biocompatible Au nanoparticle and Mg-Fe MMO nanosheet (Au/MgFe-MMO) with well-matched energy band structure on the titanium implant to manipulate proton and electron transfer. Au or MgFe-MMO film alone will not kill bacteria and cells, so the selective antibacterial effect and mechanism based on interfering with membrane proton and electron transfer can be comprehensively explored. When the bacteria contacted the Au/MgFe-MMO film, continuous transport of protons and electrons from the respiratory chain in the bacterial membrane to the implant was observed (Fig. 1). Thus, the ATP synthesis, amino acid synthesis, and various biological processes of bacteria were disrupted, leading to bacterial death from severe starvation state. Meanwhile, this smart antibacterial surface design was also extended to other heterojunction systems, proving the universality of the as-proposed hypothesis. In addition, the Au/MgFe-MMO heterojunction film was good for both osteoblasts and fibroblasts, without inhibiting their mitochondrial function. This proposed concept of selective starvation antibacterial therapy by interfering with proton and electron transfer gives a notable perspective in designing biosafe antibacterial biomaterials.

RESULTS

Heterojunction film preparation and characterization

The preparation process of Au/MgFe-MMO film is shown in Fig. 2A. The MgFe–layered double hydroxide (LDH) nanosheet arrays were firstly grown on titanium using two-step hydrothermal treatment (fig. S1) and then were calcined at 250°C to transform to MgFe-MMO arrays. The scanning electron microscope (SEM) and atomic force microscope (AFM) images of the MgFeO-Ti sample confirm that the titanium surface was uniformly covered by a nanosheet array film with a thickness of about 400 nm (Fig. 2, B and C). The transmission electron microscope (TEM) photographs show that the MgFe-MMO nanosheets had a layered structure (Fig. 2D) and the Mg, Fe, and O elements were uniformly distributed in the nanosheets (Fig. 2E). Subsequently, Au/MgFe-MMO heterojunction films were obtained by magnetron sputtering. As seen from the SEM and AFM images of Au/MgFeO-Ti (Fig. 2, F and G), dense nanoparticles were distributed on the surface of the nanosheets. The heterostructure of Au nanoparticles and MgFe-MMO nanosheets can be also observed in the TEM high-resolution images (Fig. 2H). Au nanoparticles were distributed on the surface of MgFe-MMO nanosheets, as shown in the elemental mapping images (Fig. 2I). The x-ray photoelectron spectroscopy (XPS) and Raman spectrum also show the signals of the Au, Mg, Fe, and O elements (fig. S2) and the characteristic peaks of Au, MgO, and FeO (fig. S3). The above results confirm the successful construction of Au/MgFe-MMO heterojunction arrays on the titanium implant.

To further compare and analyze the physicochemical properties of Au/MgFe-MMO, we also prepared nano-Au films on titanium under the same conditions (fig. S4). XPS high-resolution spectrum was used to study the surface electronic structure. As shown in Fig. 3A, the peaks located at 84.6 and 88.3 eV correspond to the characteristic peaks of Au $4f_{7/2}$ and Au $4f_{5/2}$, respectively, which belong to the simple Au on Au-Ti (*41*). In addition, a very small amount of oxidized Au was detected, which may be due to the oxidization during the magnetron sputtering process. The lower binding energy of Au in the Au/MgFeO-Ti compared to the Au-Ti indicates that the Au nanoparticles in the Au/MgFe-MMO heterojunction gain electrons. That is, the introduction of MgFe-MMO reduced the valence state of Au in Au/MgFe-MMO. The peaks located at 711.9 and 725.6 eV correspond to the Fe $2p_{3/2}$ and Fe $2p_{1/2}$, and the peaks located at 718.9 and 731.7 eV correspond to satellite peaks of Fe, which belong to the iron oxides in MgFe-MMO (Fig. 3B) (*42*). Both the Fe $2p_{3/2}$ and Fe $2p_{1/2}$ binding energies of Fe in the Au/MgFe-MMO film are increased compared to those in MgFe-MMO films, indicating the loss of electrons of Fe in Au/MgFe-MMO. Similarly, an increase in the binding energies of Mg and O elements was observed in the Au/MgFe-MMO films compared to the MgFe-MMO film as well (Fig. 3, C and D), indicating that both Mg and O elements lost electrons. Combined with the above elemental XPS high-resolution results, it indicates that the Mg, Fe, and O lose electrons, while the Au gained electrons in the Au/MgFe-MMO heterojunction. That is, an interfacial electron transfer occurred between the MgFe-MMO nanosheets and Au nanoparticles, leading to a decrease in the binding energy of the Au element and an increase in the Mg, Fe, and O elements.

To further investigate the interfacial electronic interactions between Au and MgFe-MMO, we used ultraviolet photoelectron spectroscopy (UPS) to analyze the energy band structure of the heterojunction. As shown in Fig. 3E, the cutoff edge of MgFe-MMO is 17.15 eV, which corresponds to a work function of 4.05 eV (21.2 eV − 17.15 eV = 4.05 eV). The work function of Au is 5.1 eV, and its Fermi energy level is lower than that of MgFe-MMO. Therefore, when Au contacted MgFe-MMO, a Schottky heterojunction was formed, and the electrons were transferred from MgFe-MMO with a high Fermi energy level to the Au until a new equilibrium was reached in the Au/MgFe-MMO system, which is consistent with the XPS results. As shown in Fig. 3E, the cutoff edge of Au/MgFe-MMO is 16.83 eV, which corresponds to a work function of 4.37 eV (21.2 eV − 16.83 eV = 4.37 eV). Further, the minimum valence band positions of MgFe-MMO and Au/

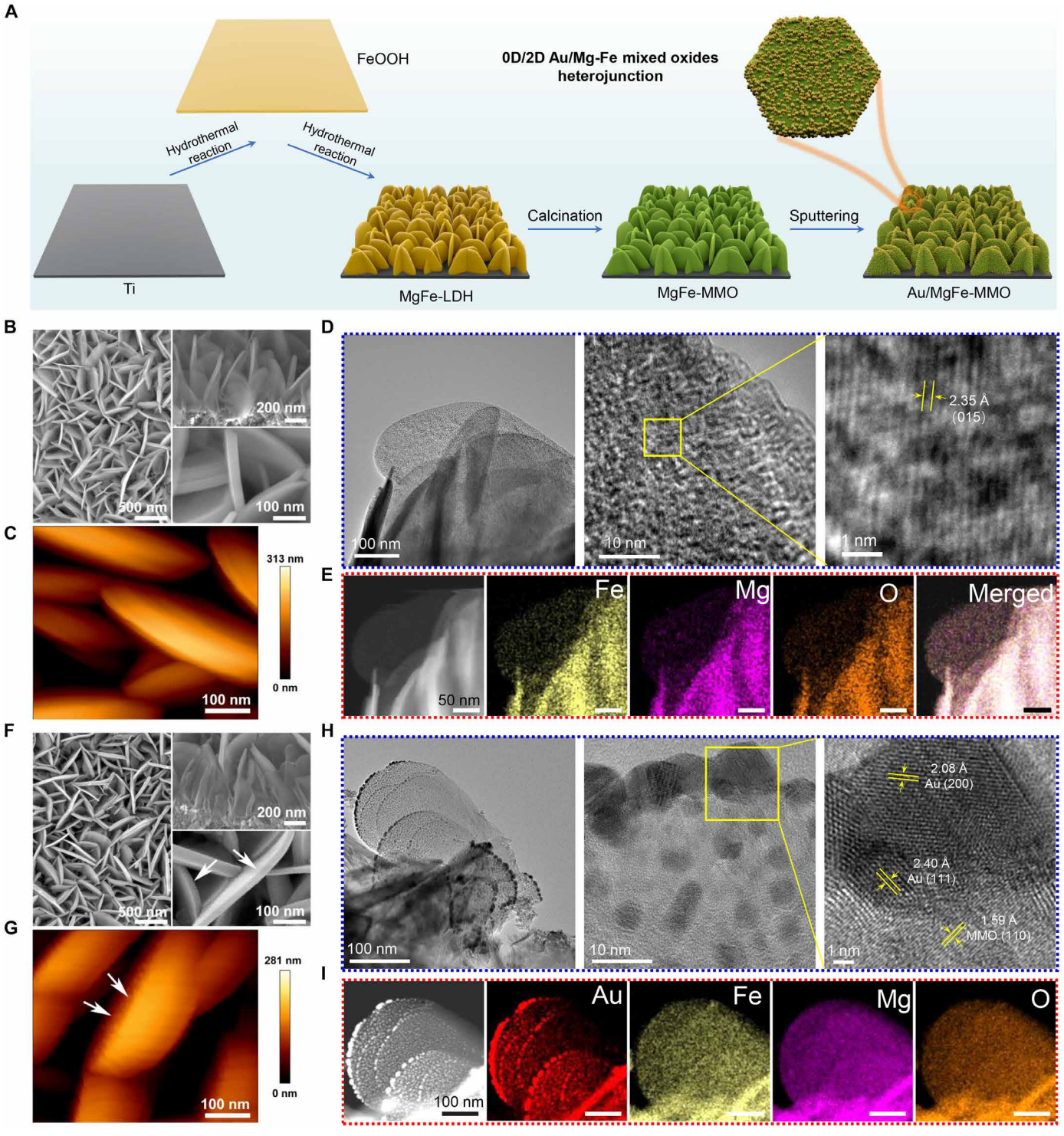

Fig. 2. Preparation and characterization of Au/MgFe-MMO heterojunction film. (**A**) The illustration of the preparation process of the Au/MgFe-MMO heterojunction film. (**B**) The surface and cross-sectional morphology of MgFeO-Ti. (**C**) The AFM three-dimensional (3D) morphology image of MgFeO-Ti surface. (**D**) The TEM high-resolution images and (**E**) the corresponding Fe, Mg, and O elemental mapping images of MgFe-MMO nanosheet. (**F**) The surface and cross-sectional morphology of Au/MgFeO-Ti. (**G**) The AFM 3D image of Au/MgFeO-Ti surface. (**H**) The TEM high-resolution images and (**I**) the corresponding Au, Fe, Mg, and O elemental mapping images of Au/MgFe-MMO nanosheet.

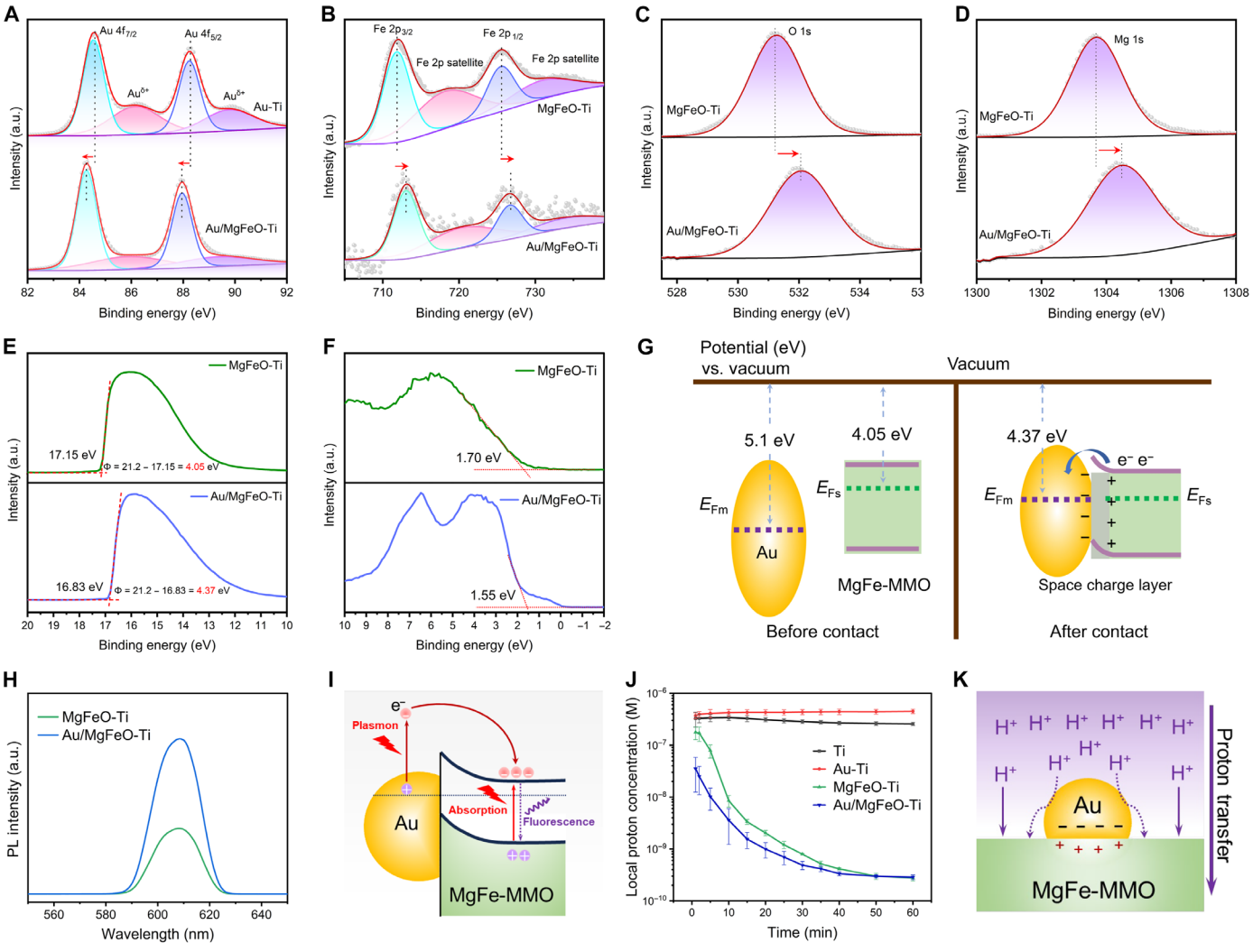

Fig. 3. Manipulation of proton and electron transfer of Au/MgFe-MMO heterojunction film. (**A**) Au 4f, (**B**) Fe 2p, (**C**) O 1s, and (**D**) Mg 1s XPS high-resolution spectra of Au-Ti, MgFeO-Ti, and Au/MgFeO-Ti. a.u., arbitrary units. (**E**) Ultraviolet photoelectron spectroscopy (UPS) spectra and (**F**) XPS valence band of MgFeO-Ti and Au/MgFeO-Ti. (**G**) Energy-band alignment schematic illustration of the Au, MgFe-MMO, and Au/MgFe-MMO Schottky heterojunction. (**H**) PL spectra of MgFeO-Ti and Au/MgFeO-Ti. (**I**) Plasmon resonance hot-electron transfer effect of Au/MgFe-MMO Schottky heterojunction. (**J**) The proton concentration of the local microenvironment on Ti, Au-Ti, MgFeO-Ti, and Au/MgFeO-Ti surfaces ($n = 3$). (**K**) Proton transfer effect of Au/MgFe-MMO Schottky heterojunction film.

MgFe-MMO can be determined from the XPS valence band spectrum (Fig. 3F) to be 1.70 and 1.55 eV, respectively. The bandgaps of MgFe-MMO and Au/MgFe-MMO can be determined from the ultraviolet-visible absorption spectrum (fig. S5) to be 2.08 and 2.04 eV, respectively. Combining the above results, it can be speculated that the electron transfer behavior of the Au/MgFe-MMO Schottky heterojunction interface is as shown in Fig. 3G. On the basis of the difference in work function between Au and MgFe-MMO, the contact caused the rearrangement of their Fermi energy levels and the bending of conduction band (*43*). Thus, a Schottky contact barrier was formed, pointing from the metal to the semiconductor interface, which makes it useful for manipulating the charge transfer. The current-voltage curves of the films were measured using the four-probe method. Both Ti and Au-Ti showed typical ohmic behavior, with the current increasing linearly with voltage, and the current of Au-Ti was relatively larger because of the better conductivity of Au (fig. S6). However, the MgFeO-Ti and Au/MgFe-MMO-Ti samples exhibited typical semiconductor current-voltage characteristic curves (fig. S7). In detail, the MgFe-MMO film exhibited a semiconductor current-voltage curve, whereas the Au/MgFe-MMO film was unidirectionally conductive to electrons within a certain voltage range due to the Schottky barrier. The above results confirm that a Schottky heterojunction film composed of Au and MgFe-MMO was successfully constructed.

The electron and proton transfer behaviors were further explored. The photoluminescence (PL) spectra were tested, and the results are shown in Fig. 3H. The emission fluorescence intensity of the Au/MgFeO-Ti was stronger than that of MgFeO-Ti under the stimulation of excitation light at a 300-nm wavelength, which may be caused by the plasmon resonance effect of Au nanoparticles. Under the illumination condition, the recombination of the electron-hole pair generated by MgFe-MMO would produce part of the fluorescence. At the same time, high-energy hot electrons were generated because of the

plasma resonance effect of Au nanoparticles, which, in turn, crossed the Schottky barrier into the conduction band of MgFe-MMO and, thus, enhanced the fluorescence of the exciton emission of MgFe-MMO (Fig. 3I). This result indicates that electron flow from gold nanoparticles to MgFe-MMO semiconductors can be realized under specific excitation conditions. This process has important implications for the bacterial behaviors, which will be discussed in the subsequent section. On the other hand, the samples were immersed in saline, and then the local proton concentration on various sample surfaces and the overall proton concentration of solution were examined using a pH microelectrode, and the results are shown in Fig. 3J. The proton concentrations on the surface of the MgFeO-Ti and Au/MgFeO-Ti are obviously lower compared to Ti and Au-Ti, confirming the proton consuming ability of MgFe-MMO and Au/MgFe-MMO. Because the MgFe-MMO nanosheets on Au/MgFeO-Ti are partially covered by Au nanoparticles (Fig. 2, F to I), the contact area between protons and the MgFe-MMO nanosheets was reduced, which weakens their ability to consume protons. However, the negatively charged Au nanoparticles would attract the protons in the solution by electrostatic action (fig. S8) and further transfer protons to the MgFe-MMO nanosheets, which, in turn, accelerated the effect of proton consumption (Fig. 3K). The above double-edged sword effect resulted in no significant difference in the local proton concentration between the MgFeO-Ti and Au/MgFeO-Ti groups, although the overall proton concentration of the saline solution in the MgFeO-Ti group was the smallest (fig. S9). The above results confirm the successful construction of Au/MgFe-MMO Schottky heterojunction film, and it has the ability to manipulate electron and proton transfer.

In vitro antibacterial performances

Both Gram-positive (*Staphylococcus aureus*) and Gram-negative (*Escherichia coli*) bacteria were used to evaluate the antibacterial performances of Au/MgFe-MMO film. As shown in Fig. 4A, compared to Ti, the number of both *S. aureus* and *E. coli* colonies on Au-Ti showed no significant change, and that on MgFeO-Ti slightly reduced. Notably, neither *S. aureus* nor *E. coli* colonies were observed on Au/MgFeO-Ti. The antibacterial rates of Au-Ti, MgFeO-Ti, and Au/MgFeO-Ti samples against *S. aureus* were −20.882, 27.787, and 99.977%, respectively (Fig. 4B), and those against *E. coli* were 11.416, 44.615, and 99.975%, respectively (Fig. 4C). These results indicate that the combination of Au and MgFe-MMO produced good synergistic broad-spectrum antibacterial performances. In addition, live/dead staining was used to further evaluate the antibacterial effect of these films, and the results are shown in Fig. 4 (D and E). The surfaces of Ti and Au-Ti were almost completely covered by live bacteria with no dead bacteria. The number of bacteria on MgFeO-Ti was reduced, but the dead bacteria were few. In addition, the number of bacteria on Au/MgFeO-Ti samples was negligible, and most bacteria were dead, which further confirmed the good antibacterial performance of Au/MgFe-MMO heterojunction film. In addition, we also observed the morphological structure of the bacteria cultured on various samples by SEM. As shown in Fig. 4F, both Ti and Au-Ti samples were covered with numerous *S. aureus*, which appeared as intact spherical shapes without any breakage. The number of *S. aureus* on the MgFeO-Ti sample was relatively reduced, but their morphology was still intact, indicating that the MgFe-MMO film only inhibited the growth of bacteria but did not kill them (this is in agreement with the results of the plate colony counting assay and the live/dead staining; Fig. 4, A and D). The number of *S. aureus* on the Au/MgFe-MMO heterojunction film was very low, and the bacterial membrane was indented, while some of the bacteria were in a completely broken state. Similarly, the growth of *E. coli* on Ti and Au-Ti samples was not obviously affected, and the bacterial membrane was intact (Fig. 4G), while the number of *E. coli* on MgFe-MMO films was low, and a small number of bacteria showed a longer morphology due to the inhibition of energy metabolism (*44*). For the Au/MgFe-MMO, more elongated *E. coli* were observed, and most of the bacteria have completely broken and collapsed (figs. S10 and S11). TEM was further used to observe the membrane structure of bacteria on Ti and Au/MgFe-MMO surfaces after 6 hours of incubation to analyze their antibacterial mechanisms, and the results are shown in Fig. 4 (H and I). The morphology of the bacterial membrane of *S. aureus* on the Ti surface was complete, the cytoplasm was free of leakage, and some bacteria in a state of division (yellow arrows) were observed, indicating that it was in a good state of growth. Comparatively, the membrane structures of most bacteria on the Au/MgFe-MMO surface were defective, and the cytoplasm was obviously leaking. For *E. coli*, a similar broken state was observed on Au/MgFe-MMO. The cytoplasmic leakage of bacteria was further examined, and the results are shown in Fig. 4 (J and K). The intracellular protein leakage of the bacteria on the Au/MgFeO-Ti was significantly higher than that of the Ti, Au-Ti, and MgFeO-Ti groups. In addition, the ROS level of bacteria on Au/MgFeO-Ti was more than 10 times higher than that of other groups (Fig. 4, L and M). ROS is strongly oxidizing and can destroy the bacterial membrane structure, proteins, and DNA substances. The above results suggest that the bacteria on Au/MgFe-MMO film may die because of the destruction of their energy metabolism, which, in turn, generates severe oxidative stress, leading to the breakage of membrane structure and the leakage of cytoplasmic proteins and other substances.

Antibacterial mechanism based on interfering with proton and electron transfer

Figure 3 shows that Au/MgFe-MMO heterojunction film has the ability to manipulate electron and proton transfer. To analyze the electron transfer effect of the film on the bacterial respiratory chain, we examined the linear voltammetric scanning (LSV) curves of the samples in the presence/absence of bacteria (*45*). When bacteria were not present, the saturation currents of Ti, Au-Ti, MgFeO-Ti, and Au/MgFeO-Ti groups were all less than 2 μA, with no significant difference (fig. S12). However, the Au/MgFeO-Ti group showed the strongest saturation current in the presence of bacteria due to the transfer of bacterial membrane electrons to the Au/MgFe-MMO film (Fig. 5A). Furthermore, the membrane electron concentration of *S. aureus* cultured on the samples was detected using 5-cyano-2,3-ditolyl tetrazolium chloride (CTC) reagent. The electrons from the respiratory transport chain of the bacterial membrane can reduce the CTC reagent to substance B to emit red fluorescence, while the bacterial DNA can bind to the 4′,6-diamidino-2-phenylindole (DAPI) reagent to emit blue fluorescence (*46*). As shown in Fig. 5B, strong blue and red fluorescence was detected on Ti, indicating that the respiratory electron transfer chain worked normally, while the membrane electron concentrations of bacteria on Au-Ti and MgFeO-Ti were relatively reduced. Very faint red fluorescence was observed on Au/MgFeO-Ti, indicating that bacterial respiratory chain electron transfer was severely disrupted. As shown in Fig. 5C, the bacteria rely on the operation of the respiratory electron transfer chain on the membrane to provide energy, which makes the bacterial membrane exhibit n-type semiconductor properties (*26*). When the bacteria were

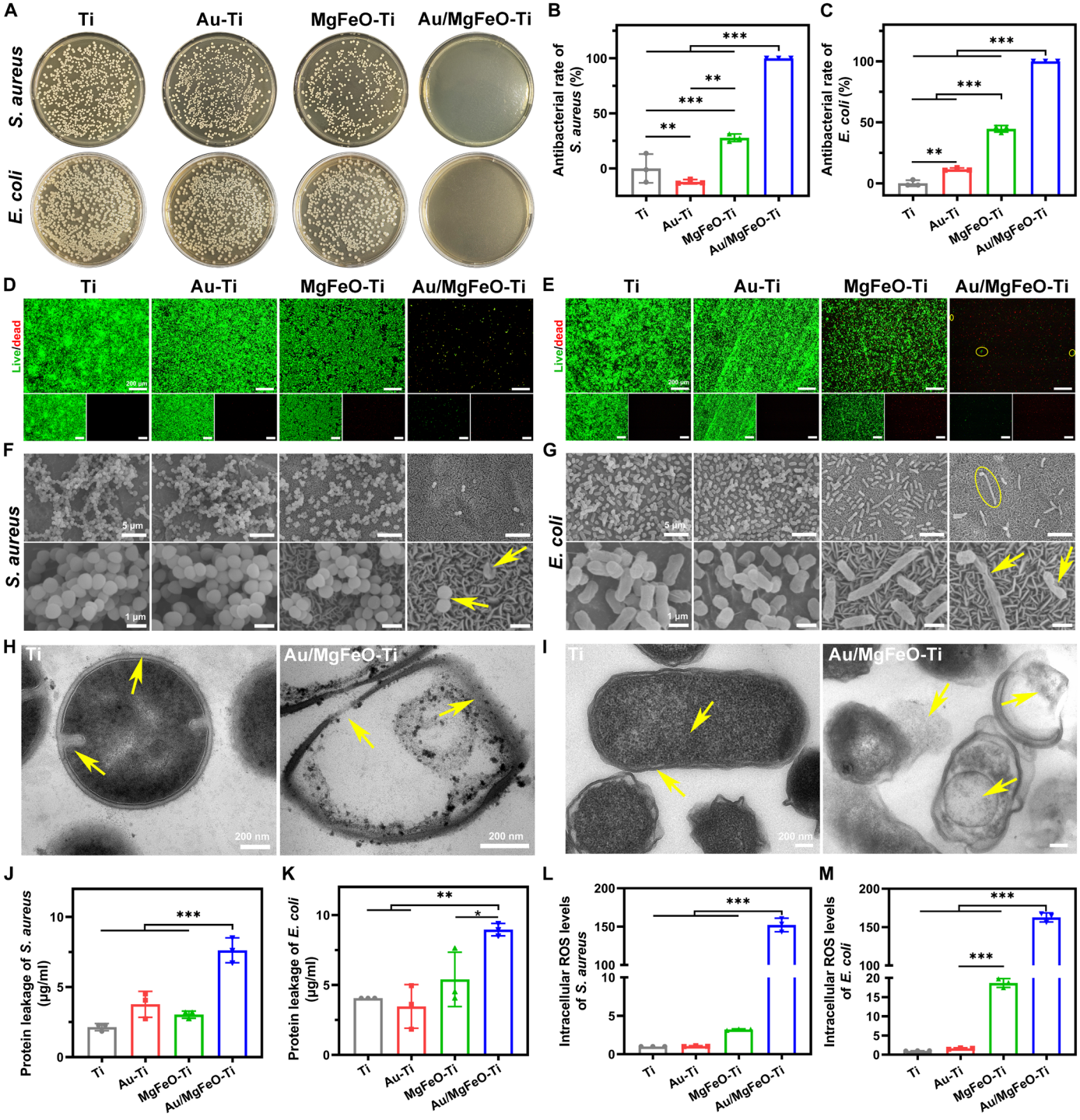

Fig. 4. In vitro antibacterial performances of Au/MgFe-MMO heterojunction film. (**A**) Photos of bacterial colonies and the corresponding antibacterial rates against (**B**) *S. aureus* and (**C**) *E. coli* of various samples ($n = 3$). Live/dead staining images of (**D**) *S. aureus* and (**E**) *E. coli* cultured on various samples. SEM morphology of (**F**) *S. aureus* and (**G**) *E. coli* cultured on various samples. TEM morphology of (**H**) *S. aureus* and (**I**) *E. coli* cultured on various samples. Protein leakage of (**J**) *S. aureus* and (**K**) *E. coli* cultured on various samples ($n = 3$). Intracellular ROS level of (**L**) *S. aureus* and (**M**) *E. coli* cultured on various samples ($n = 3$). $^{**}P < 0.01$ and $^{***}P < 0.001$.

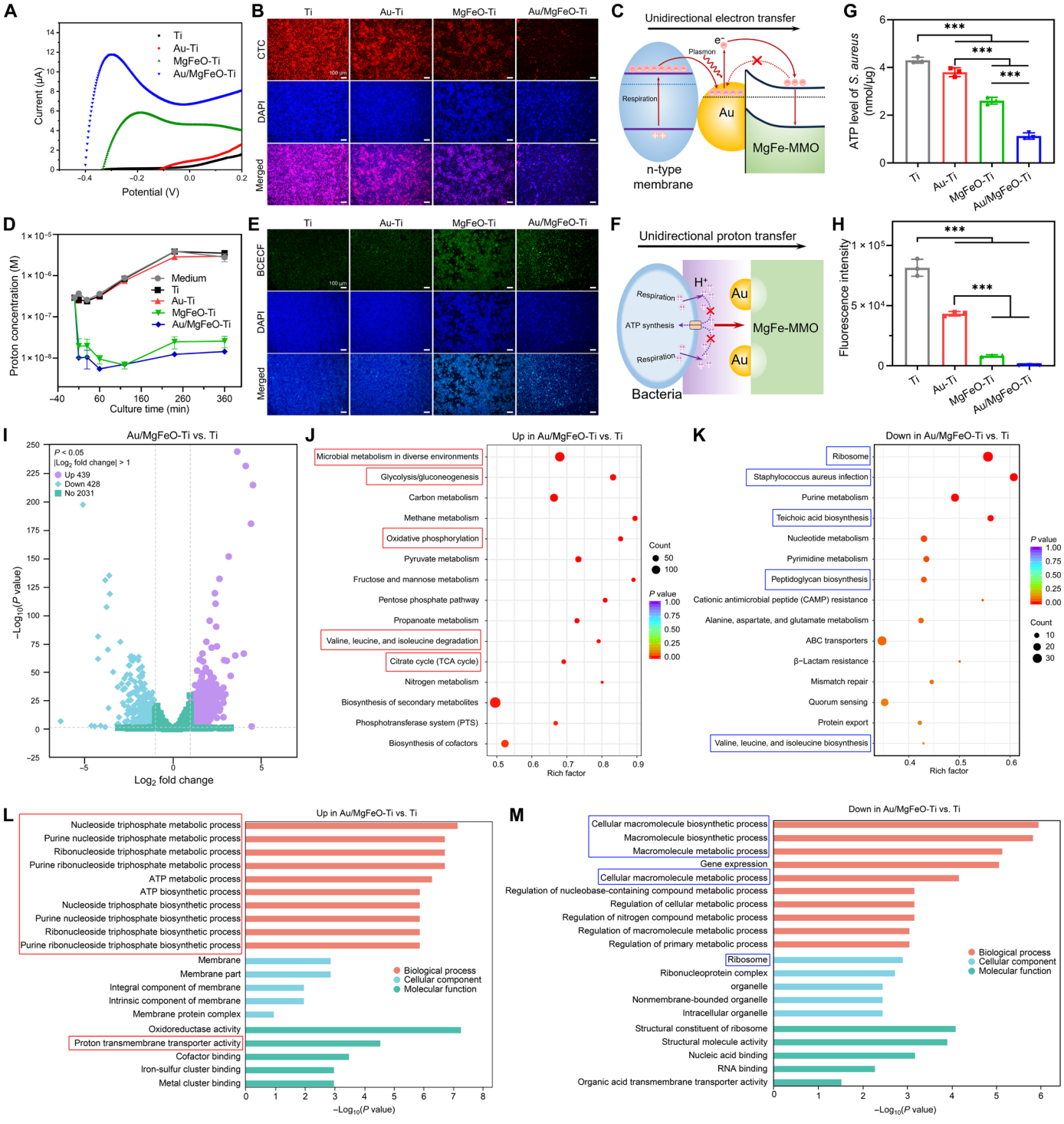

Fig. 5. Antibacterial effect of Au/MgFe-MMO heterojunction film based on interfering with proton and electron transfer on the bacterial membrane. (**A**) LSV curves of various samples in the presence of *S. aureus*. (**B**) CTC/DAPI staining images of *S. aureus* cultured on various samples for 6 hours. (**C**) Schematic illustration of electron transfer from the bacterial membrane to the Au/MgFe-MMO heterojunction film. (**D**) Extracellular proton concentration ($n = 4$) and (**E**) BCECF/DAPI staining images of *S. aureus* cultured on various samples for 6 hours. (**F**) Schematic illustration of proton transfer from the bacteria to the Au/MgFe-MMO heterojunction film. (**G**) Bacterial activities and (**H**) ATP level of *S. aureus* cultured on various samples for 6 hours ($n = 3$). (**I**) Volcano plot of transcriptomic analysis of differentially expressed genes. (**J**) Up-regulated and (**K**) down-regulated Kyoto Encyclopedia of Genes and Genomes (KEGG) enrichment analysis in Au/MgFeO-Ti versus Ti group. TCA, tricarboxylic acid; ABC, ATP-binding cassette. (**L**) Up-regulated and (**M**) down-regulated Gene Ontology (GO) enrichment analysis in Au/MgFeO-Ti versus Ti group. ***$P < 0.001$.

in contact with the Au/MgFe-MMO heterojunction, the electrons may be transferred from the bacterial membrane to the Au nanoparticles due to the normalization of the Fermi energy level, so the electronic state density of Au nanoparticles was increased (*47*). At the same time, the loss of electron energy may cause a fluorescence excitation–like effect, resulting in the emergence of high-energy hot electrons in the Au nanoparticles (*48*). These hot electrons flowed across the Schottky barrier formed by the Au/MgFe-MMO heterojunction into the conduction band of MgFe-MMO and subsequently jumped into the valence band of MgFe-MMO. This process led to a continuous loss of electrons in the respiratory chain of the bacterial membrane, which, in turn, negatively affected bacterial respiratory metabolic process.

On the other hand, most bacteria have to maintain an externally high and internally low transmembrane PMF to drive the synthesis of the energy-currency ATP. To investigate the effect of Au/MgFe-MMO on the PMF, we detected the extracellular proton concentration of bacteria cultured on various samples for 6 hours using a pH microelectrode. With the extension of incubation time, the concentration of protons in the bacterial extracellular microenvironment on Ti and Au-Ti remarkably increased to 3.51×10^{-6} and 2.96×10^{-6}, respectively (Fig. 5D). Under normal survival conditions, *S. aureus* will acidify the extracellular environment by pumping out protons through respiration reaction, which, in turn, enhances the transmembrane PMF to synthesize more ATP. Inversely, the bacterial extracellular proton concentration of MgFe-MMO and Au/MgFe-MMO groups decreased by more than a factor of 10, to 2.57×10^{-8} and 1.44×10^{-8}, respectively, which would impede the flow of extracellular proton into the bacteria to synthesize ATP. The intracellular proton concentration was further evaluated by fluorescent probe of 2′,7′-bis(2-carboxyethyl)-5(6)-carboxyfluorescein acetoxymethyl ester (BCECF-AM). The stained bacteria on the MgFe-MMO and Au/MgFe-MMO emitted stronger green fluorescence signals compared to Ti and Au-Ti, indicating that their intracellular proton concentration was remarkably lower (Fig. 5E), which further confirmed the blocked reflux of protons into the bacteria. Overall, MgFe-MMO and Au/MgFe-MMO continuously consumed protons in the local microenvironment, so the transmembrane PMF of bacteria was weaken, leading to the blockage of ATP synthesis (Fig. 5F). On the basis of the above dual disruption of the proton and electron transfer processes, the energy metabolism of bacteria was severely inhibited, resulting in a continuous starvation state. Thus, the ATP content level of the bacteria on the Au/MgFe-MMO film was the lowest (Fig. 5G and fig. S13), and the bacterial activity was almost completely lost (Fig. 5H and fig. S14). The above results indicate that the energy metabolism of the bacteria on the Au/MgFe-MMO film was severely damaged.

Gene transcriptomics was further used to analyze the genes expression of bacteria. Compared with Ti, 439 genes were up-regulated and 428 genes were down-regulated in *S. aureus* on the Au/MgFe-MMO film, indicating that their metabolic state remarkably changed (Fig. 5I). Kyoto Encyclopedia of Genes and Genomes (KEGG) enrichment analysis showed that the bacterial glycolysis/gluconeogenesis, oxidative phosphorylation, tricarboxylic acid cycle, carbon metabolism, nitrogen metabolism, and fructose and mannose metabolic pathways were obviously up-regulated (Fig. 5J), indicating that the energy metabolism of the bacteria was greatly affected. In addition, the degradation of valine, leucine, and isoleucine underwent a distinct increase. As three essential amino acids for *S. aureus*, their degradation would affect the protein synthesis of the bacteria. However, their degradation products, succinyl coenzyme A and acetyl–coenzyme A, could enter the Krebs cycle to produce energy and gluconeogenesis, which are beneficial for their survival in a nutrient-limited environment (*49*). The above results suggest that *S. aureus* on Au/MgFe-MMO may have to up-regulate energy metabolism–related genes and catabolize proteins for energy supply to sustain their life due to impaired energy metabolism. That is to say, the bacteria on Au/MgFe-MMO film were in starvation state. On the other hand, the down-regulated metabolic pathways include ribosome, peptidoglycan biosynthesis, and teichoic acid biosynthesis (Fig. 5K). Ribosomal protein synthesis and other metabolic activities are highly energy-consuming cellular processes (*50*), and the low expression of related genes can reduce biosynthesis and save energy, which is favorable for the survival of bacteria in starvation state. Further analysis of the Gene Ontology (GO) gene enrichment results showed that the up-regulated gene functions of *S. aureus* on the Au/MgFe-MMO surface were mainly focused on the metabolism of energy molecules (fig. S15). For example, ATP synthesis and metabolism, nucleoside triphosphate, and purine nucleoside triphosphate synthesis and metabolism were obviously up-regulated (Fig. 5L). The down-regulated gene functions were mainly focused on the synthesis and metabolism of biofunctional macromolecules (fig. S16), such as the synthesis of nitrogen compounds, nucleobase-containing compounds, and RNA (Fig. 5M). These further confirm that the bacterial energy metabolism was inhibited and the nonsurvival essential metabolic genes had to be down-regulated, while the energy synthesis–related functional genes and signaling pathways were up-regulated to maintain the life-essential energy supply. In addition, we unexpectedly found significant down-regulation of the infection-related pathways of *S. aureus* on the Au/MgFe-MMO (Fig. 5J), suggesting that its toxicity would be weakened under starvation, which would reduce the damage to the human body.

Further analysis of bacterial metabolic changes using gene set enrichment analysis revealed that the expression of genes related to bacterial response to oxidative stress was enhanced on the Au/MgFe-MMO film (Fig. 6A). On one hand, the disruption of the proton and electron transfer process in the respiratory chain of the bacterial membrane led to electron leakage and the generation of ROS (*46*). Meanwhile, because of the energy scarcity, bacteria may increase the utilization of carbon sources or the consumption of oxygen to produce more ATP through oxidative phosphorylation, which may lead to the generation of excessive ROS. The above changes made the bacteria in a state of severe oxidative stress, so the process of oxidation-reduction reactions and oxidoreductase activity were enhanced (Fig. 6, B and C). The ROS with high reactivity would damage the intracellular DNA and other molecules of bacteria (*51*), which leads to the up-regulation of cellular response to DNA stimulus and DNA repair–related genes to repair DNA (Fig. 6D).

Taking the above results together, a schematic diagram of the antibacterial mechanism based on the disruption of bacterial energy metabolism by interfering with proton and electron transfer is illustrated in Fig. 6E. When the bacteria contacted the Au/MgFe-MMO heterojunction film, the electrons and protons in the respiratory chain of the bacterial membrane in contact with the film were continuously transferred to the implant, leading to the disruption of the respiratory chain. In turn, the ATP synthesis was blocked and energy was scarce, leading the bacteria to a state of severe starvation. For the part of the bacteria that is not in contact with the film, it may not be able to capture protons and electrons efficiently. Therefore, that part of the

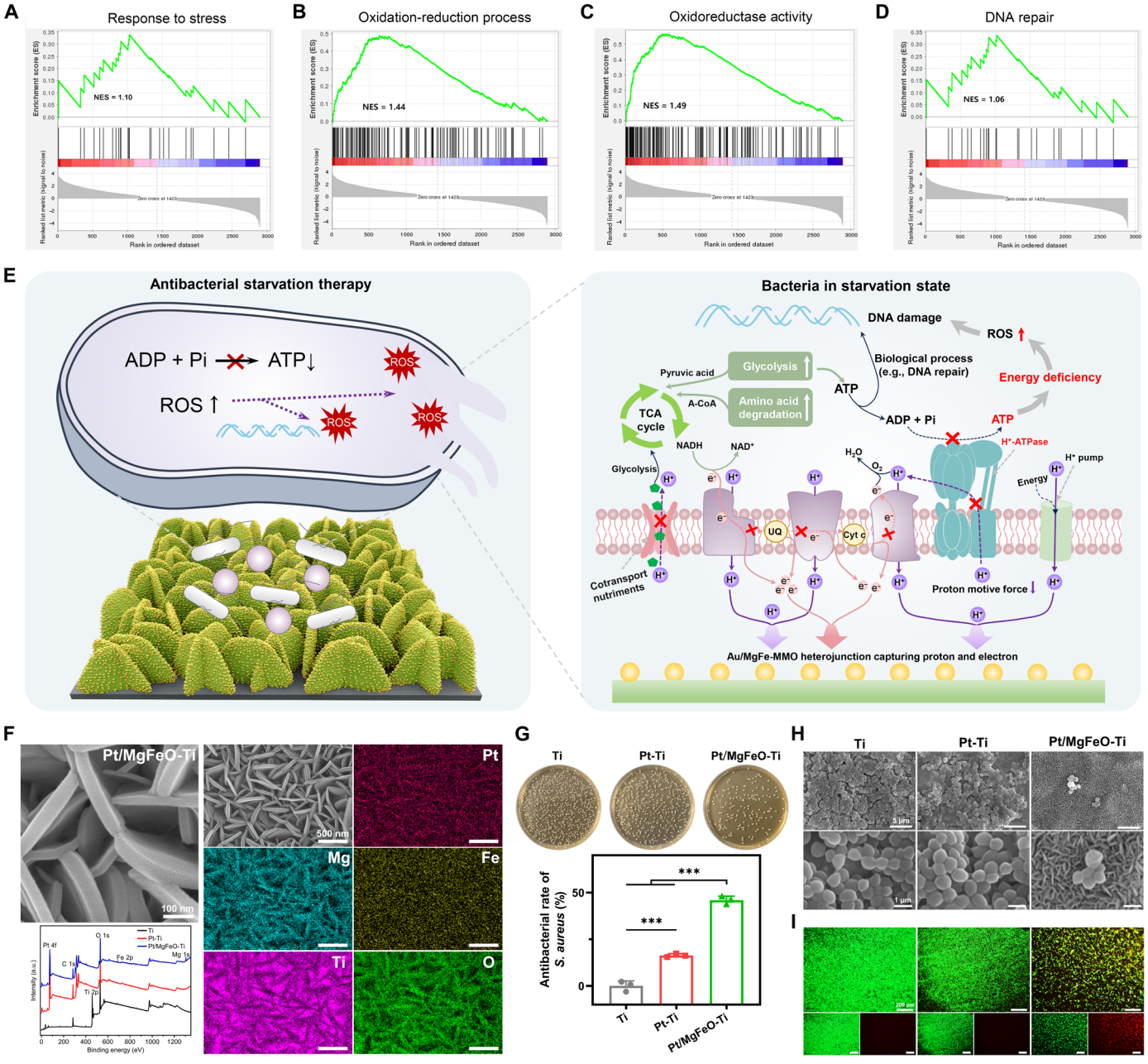

Fig. 6. Antibacterial mechanism and the extension of metal/MMO Schottky heterojunction. Gene set enrichment analysis of (**A**) response to stress, (**B**) oxidation-reduction process, (**C**) oxidoreductase activity, and (**D**) DNA repair. NES, normalized enrichment score. (**E**) Starvation antibacterial mechanism of Au/MgFe-MMO heterojunction film based on interfering with proton and electron transfer. ATPase, adenosine triphosphatase; A-CoA, acetyl–coenzyme A. (**F**) The characterization of Pt/MgFe-MMO heterojunction film. (**G**) The antibacterial performance of Pt/MgFe-MMO against *S. aureus* ($n = 3$). (**H**) The SEM morphology and (**I**) live/dead staining images of *S. aureus* cultured on Pt/MgFe-MMO heterojunction film. ***$P < 0.001$.

respiratory chain of the bacteria may still work, which is why the bacteria can survive for some time. However, because of the energy deficit, bacteria have to accelerate the respiratory chain, and more electron leakage from this process can lead to the production of ROS. In addition, because protons cannot flow into the bacteria, there are not enough protons to react with the electrons and oxygen in the bacterial respiratory chain to produce water, so that electrons and oxygen may also react to produce more ROS (*46*). As a result, the level of ROS in the bacteria increased and oxidative stress occurred, leading to the destruction of DNA and membrane structure and death.

To verify the universality of this antibacterial heterojunction design based on interfering with proton and electron transfer, we further constructed a similar Pt/MgFe-MMO Schottky heterojunction film (Fig. 6F). The electron and proton transfer behaviors similar to those of Au/MgFe-MMO film were also proved (fig. S17 and S18). The results of bacterial experiments showed that the combination of

Pt and MgFe-MMO produced significant synergistic antibacterial effects against *S. aureus* (Fig. 6, G and H) and *E. coli* as well (figs. S19 and S20). It further confirms our proposed antibacterial concept of disrupting bacterial energy metabolism based on interfering with bacterial membrane proton and electron transfer.

Osteoblast responses and in vivo anti-infection and bone formation

Osteoblasts were selected to evaluate the biocompatibility of Au/MgFe-MMO heterojunction film–modified titanium implants. As shown in Fig. 7A, the osteoblasts (MC3T3-E1) adhered and spread well on all samples at 4 and 24 hours. The intracellular mitochondrial membrane potential of osteoblasts was further detected using JC-1 fluorescent probe. Different from bacteria, the intracellular mitochondrial membrane potential of MC3T3-E1 cells on all sample did not decrease (Fig. 7B), indicating that the cellular respiration and metabolism were normal. This indicates that the Au/MgFe-MMO heterojunction film can selectively inhibit the respiratory chain of bacteria and cannot affect the mitochondrial energy metabolism of normal cells. The live/dead staining and SEM results showed that all samples were almost completely covered by live cells without dead cells (Fig. 7, C and D). The proliferative activity of MC3T3-E1 cells was further examined using alamarBlue reagent, and the results are shown in Fig. 7E. At 4 and 7 days, the proliferation rate of MC3T3-E1 cells on Au-Ti was slightly lower than that of Ti, while the proliferation rate of MgFeO-Ti and Au/MgFeO-Ti groups was significantly higher than that of Ti. This may be attributed to the positive effect of the local weakly alkaline microenvironment and the built-in electric field generated by the Au/MgFe-MMO on the osteoblasts (*38*, *52*). These results confirm that the Au/MgFe-MMO heterojunction film has good cytocompatibility for osteoblasts.

A rat osteomyelitis model was further constructed to evaluate the in vivo antibacterial and osseointegration effects of Au/MgFe-MMO heterojunction–modified titanium implant under infection conditions (Fig. 7F). After implantation for 1 week, the implants were removed and the antibacterial effect was evaluated. As shown in Fig. 7G, the medium containing Ti implant showed a turbidity state, and the number of plate colonies was high, indicating that the Ti surface was covered by a large number of bacteria. The medium of Au/MgFeO-Ti group remained clear, and the bacterial colonies were less, with a corresponding antibacterial rate of 95.42% (Fig. 7H). The Giemsa and hematoxylin and eosin (H&E) staining images of the tissue around the implant are shown in Fig. 7I. The number of bacteria in the tissues around the Au/MgFeO-Ti implant was obviously reduced compared to Ti. The H&E staining images show that the number of inflammatory cells in the tissues was relatively low and the bacterial infection was slight, indicating that the Au/MgFeO-Ti implant can effectively inhibit the initial bacterial infection. After implantation for 6 weeks, the new bone formed on the implant surface was analyzed using micro–computed tomography (micro-CT), and the 3D reconstruction results are shown in Fig. 7J. Compared with Ti, the amount of new bone generated on Au/MgFeO-Ti was obviously more, and the corresponding bone-implant contact rate and bone volume (BV)/tissue volume (TV) were also obviously higher than those of Ti group (Fig. 7, K and L).The Van Gieson (VG) staining results also confirmed that more new bone was formed on the Au/MgFeO-Ti surface (Fig. 7M). In summary, the Au/MgFe-MMO film could promote osseointegration under infection conditions and also have good biosafety (fig. S21).

Fibroblast responses and in vivo anti-infection and soft tissue sealing

Apart from bone tissue, implants are often used as percutaneous implantable devices in direct contact with soft tissue. Fibroblasts play an important role in soft tissue repair, so they were also used to evaluate biocompatibility of as-prepared films. As shown in Fig. 8 (A and B), the initial adhesion and intracellular mitochondrial membrane potential of fibroblasts (L929) on Ti, Au-Ti, MgFeO-Ti, and Au/MgFeO-Ti were not inhibited as well. In addition, all sample surfaces were fully covered by live cells, and no dead cells were observed (Fig. 8, C and D). There was no significant difference in the proliferative activity of fibroblasts among all groups at 1 and 7 days (Fig. 8E). The proliferation rate of L929 cells on Au/MgFeO-Ti was slightly higher than that on the Ti at 4 days, which may be attributed to the built-in electric field generated by Au/MgFe-MMO and the bioactive Mg ions promoting the proliferation of fibroblasts (*53*). The above results confirm that the Au/MgFe-MMO heterojunction film has good cytocompatibility for fibroblasts as well.

A percutaneous infection model was constructed by implanting samples cocultured with bacteria into the back of mice to evaluate the in vivo anti-infection effect and soft tissue integration performance of Au/MgFe-MMO (Fig. 8F). At 1 day of implantation, a large number of bacteria existed on Ti implant, while the number on Au/MgFeO-Ti implant was obviously lower (Fig. 8G). After 4 days, the number of bacteria on Ti implant was obviously increased, while that on Au/MgFeO-Ti implant was further decreased. The corresponding antibacterial rates of Au/MgFeO-Ti were 94.196 and 99.179%, respectively (Fig. 8H). H&E and Giemsa staining results (Fig. 8, I and J) showed an obvious reduction in the number of inflammatory cells and bacteria in the soft tissues surrounding Au/MgFeO-Ti implant compared to Ti. After 4 days of implantation, the number of inflammatory cells and bacteria around Ti implant further increased, and the inflammation caused by bacterial infection intensified. Whereas fewer inflammatory cells were present in the soft tissues around the Au/MgFeO-Ti implant, the presence of bacteria was almost invisible, which suggests that the Au/MgFe-MMO film can effectively inhibit bacterial infection at the initial stage. After 7 and 14 days of implantation, Masson and vascular endothelial growth factor (VEGF) staining was performed to evaluate the effect of implant integration with soft tissues. As shown in Fig. 8 (K and L), the collagen secretion and VEGF secretion around Au/MgFeO-Ti implant increased obviously. These were conducive to the integration of the soft tissues at the wound and the implant, thus inhibiting the entry of bacteria from the external environment into the internal tissues to cause infection. The H&E staining images of the heart, liver, spleen, lung, and kidney (fig. S22) also confirmed that the Au/MgFe-MMO heterojunction film has good in vivo biosafety. Except for hard and soft tissue cells, the immune cells such as macrophages also play an important role in the human body. This Au/MgFe-MMO heterojunction film not only showed no toxicity to macrophages (RAW 264.7) but also promoted their proliferation (fig. S23). To sum up, the as-prepared heterojunction film has a good application prospect in preventing IAIs.

DISCUSSION

This study proposes an innovative strategy based on interfering with bacterial proton-electron transfer to achieve antibacterial effects, which was defined as antibacterial starvation therapy. To realize the

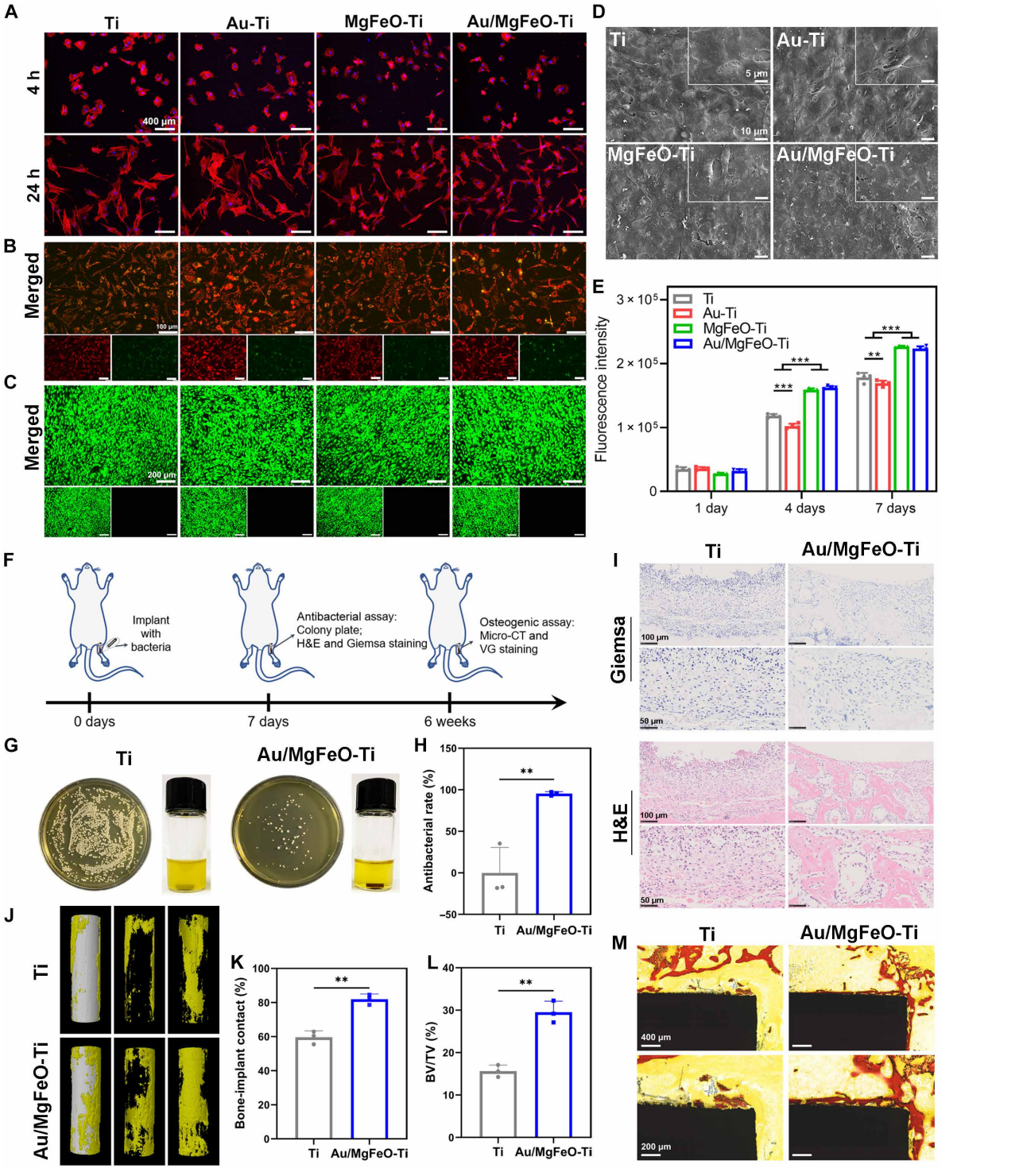

Fig. 7. Cytocompatibility to osteoblast in vitro and anti-infection and bone-repair performances in vivo of Au/MgFe-MMO heterojunction. (**A**) Cytoskeletal images of MC3T3-E1 cells on various samples for 4 and 24 hours (h). (**B**) JC-1 staining (mitochondrial membrane potential), (**C**) live/dead staining, and (**D**) SEM morphology images of MC3T3-E1 cells cultured on various samples. (**E**) Proliferation rate of MC3T3-E1 cells on various samples ($n = 4$). (**F**) Diagram of animal experiment. (**G**) Photograph of bacterial colonies and the Nutrient Broth No. 2 (NB) medium containing Ti and Au/MgFeO-Ti after implantation for 7 days. (**H**) Antibacterial rate of Au/MgFeO-Ti in vivo ($n = 3$). (**I**) Giemsa and hematoxylin and eosin (H&E) staining of bone tissues around the implants ($n = 3$). (**J**) 3D images of the reconstructed bone and implant, (**K**) bone-implant contact ratio, and (**L**) bone volume (BV)/tissue volume (TV) values measured by micro–computed tomography (micro-CT) ($n = 3$). (**M**) VG staining images of new bones around the implants. $^{**}P < 0.01$ and $^{***}P < 0.001$.

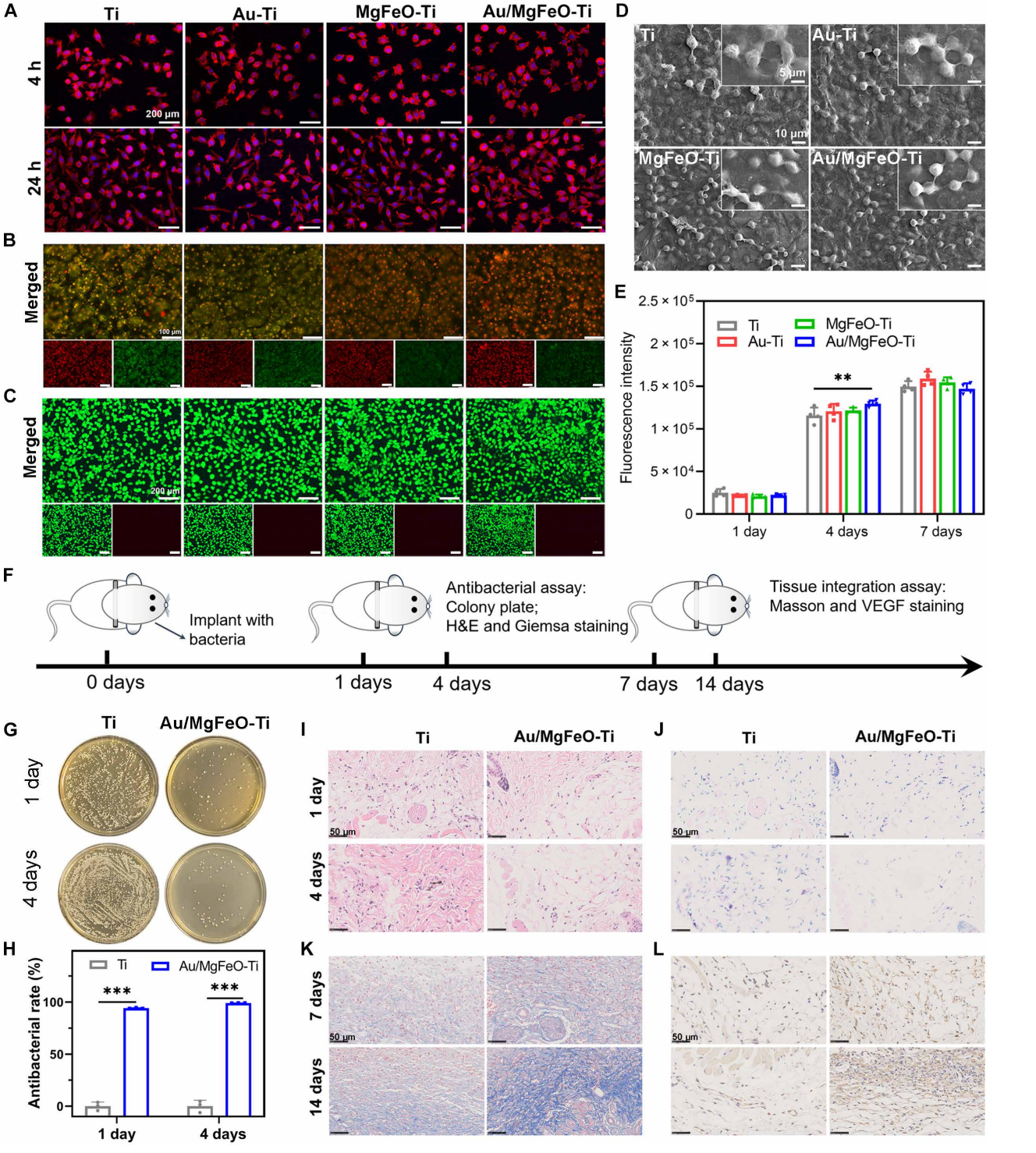

Fig. 8. Cytocompatibility to fibroblast in vitro and the anti-infection and soft tissue repair performances in vivo of Au/MgFe-MMO heterojunction. (**A**) Cytoskeletal images of L929 cells on various samples for 4 and 24 hours. (**B**) JC-1 staining (mitochondrial membrane potential), (**C**) live/dead staining, and (**D**) SEM morphology images of L929 cells cultured on various samples. (**E**) Proliferation rate of L929 cells on various samples ($n = 4$). (**F**) Diagram of animal experiment. (**G**) Photograph of bacterial colonies and (**H**) the corresponding antibacterial rate of Au/MgFeO-Ti in vivo ($n = 3$). (**I**) H&E and (**J**) Giemsa staining images of soft tissues around the implants at 1 and 4 days. (**K**) Masson and (**L**) VEGF staining images of soft tissues around the implants at 7 and 14 days. $^{**}P < 0.01$ and $^{***}P < 0.001$. h, hours.

interference of proton and electron transfer, a Schottky heterojunction film composed of zero-dimensional (0D) Au nanoparticles and 2D MgFe-MMO nanosheet arrays was tailored on titanium. On the basis of the plasma resonance effect of Au nanoparticles and the Schottky barrier, the electrons were captured and unidirectionally transferred from the bacterial membrane to the film, interfering with the step-by-step transfer of electron in the bacterial respiratory chain. Meanwhile, because of the proton-depleting effect of Mg and Fe MMOs on the local microenvironment, it impedes the flow of bacterial extracellular protons to intracellular. Under the synergistic effect of the above two aspects, the energy-currency ATP synthesis process was hindered, and the process of transmembrane nutrient cotransport was also inhibited, leading to a severe starvation state of bacteria. As a result, the bacterial ribosome function was inhibited, and many energy-consuming processes including the biosynthesis of proteins and some membrane biomolecules such as peptidoglycan and teichoic acid were blocked, so that the bacterial growth was remarkably inhibited. Moreover, the bacterial intracellular ROS level increased, and the DNA and membrane components were damaged because of severe oxidative stress. The above principle of antibacterial starvation therapy based on interfering with proton and electron transfer was also validated in the Pt/MgFe-MMO system, confirming its universality. On the other hand, the adhesion, proliferation, and mitochondrial function of both osteoblasts and fibroblasts were not affected because the proton-coupled respiratory electron transport chain of the mammalian cells is located in the intracellular mitochondria, which do not directly contact with the extracellular environment. Therefore, Au/MgFe-MMO heterojunction film does not directly interfere with the energy metabolism of cells. In addition, bacteria are about 1 μm in size, while the cells are tens of micrometers in size. Relatively speaking, bacteria are less resistant to environmental physical and chemical stimuli than cells. In summary, the selective antibacterial effects of Au/MgFe-MMO heterojunction film were attributed to the differences in membrane function and size between cells and bacteria. Furthermore, both rat osteomyelitis and mouse percutaneous infection models also confirmed that the Au/MgFe-MMO heterojunction film has good biosafety and can effectively kill bacteria and promote soft and hard tissue integration in the case of infection.

The orderly transfer of proton and electron plays a key role in the energy metabolism of living organisms (*54*–*56*). Therefore, designing biomaterials with proton-electron transfer manipulation capability is expected to enable the specific regulation of biological behaviors to conquer specific biomedical challenges. This study provides a promising smart biomaterial design reference, demonstrating that an appropriate Schottky heterojunction composed of biocompatible Au and MgFe mixed oxides can achieve excellent antibacterial effects without damaging or even enhancing cell activity. The results also showed that both Au/MgFe-MMO and Pt/MgFe-MMO heterojunction films can manipulate proton and electron transfer to realize bacteria-killing, but their antibacterial effects varied because of the different work function of Au and Pt, and the underlying mechanism remains to be further investigated. Obviously, there is a lot of room in terms of the size, distribution, and component of metal nanoparticles and MMOs of Schottky heterojunctions. These factors have an important influence on the proton-electron transfer behavior of heterojunctions to affect their antibacterial effect. Besides, a variety of in situ characterization and dynamic monitoring techniques is still needed to accurately analyze the interactions between bacteria/cells and materials, as well as the changes in various substances and energy metabolic processes of bacteria/cells. We believe that in the future, optimal antibacterial and tissue repair performances can be achieved by designing a series of heterojunction with different energy band structures and the related biological mechanisms could be deeply clarified. These materials that can regulate proton and electron transfer are not limited to film and Schottky heterojunction, and other systems such as nanomaterials and electroactive materials are promising candidates as well. Moreover, a biosafe antibacterial material that combines contact- and release-based bacterial-killing functions could be designed to achieve better therapeutic effects on IAIs in the future. In addition, the stability of film must also be taken into important consideration because the long-term stability of biomedical implant is the basis for its good service performance. In summary, this proposed concept of starvation antibacterial therapy based on interfering with proton and electron transfer gives a notable perspective on designing biosafe antibacterial biomaterials.

MATERIALS AND METHODS

Materials

Commercial pure titanium sheets and rods were purchased from Xi'an Saitismai Titanium Industry Co. Ltd. Sodium chloride [NaCl; analytical reagent (AR)], ferric chloride ($FeCl_3·6H_2O$; AR), sodium sulfate (Na_2SO_4; AR), magnesium chloride ($MgCl_2·6H_2O$; AR), and potassium hydroxide (KOH; AR) were purchased from Sinopharm Group Chemical Reagent Co. Ltd. Nitric acid (HNO_3; guaranteed reagent (GR), 65 to 68%) and hydrofluoric acid (HF; GR, ≥40%) were purchased from Shanghai Lingfeng Chemical Reagent Co. Ltd. Gold (Au; 99.999%) and platinum (Pt; 99.999%) target purchased from China New Metal Materials Technology Co. Ltd. Polyethyleneimine (PEI; 8K), Luria-Bertani (LB) and Nutrient Broth No. 2 (NB) media, CTC and BCECF-AM, and 2′,7′-dichlorodihydrofluorescein diacetate (DCFH-DA) were purchased from Sigma-Aldrich. DAPI, tetramethylrhodamine phalloidin, α–minimum essential medium, newborn calf serum (New Zealand origin), the LIVE/DEAD BacLight kit (L13152), alamarBlue, and the Pierce Bicinchoninic Acid (BCA) Protein Assay Kit were purchased from Thermo Fisher Scientific. The JC-1 Mitochondrial Membrane Potential Assay Kit and the Enhanced ATP Assay Kit were purchased from Beyotime Biotechnology.

Sample preparation

First, the titanium sheet (10 mm by 10 mm by 1 mm) or rod (Φ2 mm by 8 mm and Φ2 mm by 20 mm) was treated with a mixed solution of HF and HNO_3 to clean the surface, with the volume ratio of $HF:HNO_3:H_2O$ being 1:5:34. The as-prepared sample was denoted as Ti. Ti was placed in a hydrothermal kettle, and 50 ml of a mixed solution containing $FeCl_3$, PEI, and Na_2SO_4 was added. Subsequently, the hydrothermal reactor was placed in an electrothermostatic blast oven at 160°C for 30 min to in situ grow a FeOOH film on the Ti surfaces, and the obtained samples were labeled as FeOOH-Ti. Then, the FeOOH-Ti samples and 50 ml of a solution containing 4 mM KOH and 30 mM $MgCl_2$ were placed in a hydrothermal kettle and reacted at 160°C for 24 hours to prepare a MgFe-LDH film. The obtained samples were denoted as MgFe-LDH-Ti. The MgFe-MMO film was obtained by thermally induced transformation from the MgFe-LDH-Ti sample at a calcination temperature of 250°C for 2 hours, and the obtained sample was denoted as MgFeO-Ti. A pure Au target was used to construct Au nanoparticles on the MgFe-MMO film and Ti by magnetron

sputtering technique. The magnetron sputtering parameters were 10 mA and 80 s, and the obtained samples were denoted as Au/MgFeO-Ti and Au-Ti, respectively. Pt/MgFeO-Ti and Pt-Ti samples were prepared using Pt targets under the same magnetron sputtering condition parameters.

Sample characterization

SEM (SU8220, Hitachi, Japan) with an energy-dispersive spectrometer equipment was used to observe the surface and cross-sectional morphology of various films and analyze the surface element distribution. AFMs (Multimode 8, Bruker, Germany) were used to observe the 3D structure and potential of the sample surface. TEM (JEM-F200, JEOL, Japan) was used to observe the crystal structure and element distribution of the film. XPS and UPS measurements (AXIS Supra, Kratos Analytical Inc.) were used to detect the element composition, valence state, and valence state spectrum of these films with a monochromatized Al Kα radiation (hv = 1486.69 eV, 225 W) source, and the work functions of the MgFe-MMO and Au/MgFe-MMO films were measured with an unfiltered He-discharge lamp (21.22 eV). Raman spectrum of various samples was detected by a Raman microscope system (LabRAM, Horiba Jobin Yvon, France). Ultraviolet and visible spectrophotometer (Lambda 750, PerkinElmer) was used to detect the bandgap of the MgFe-MMO and Au/MgFe-MMO films.

Evaluation of proton-electron transfer regulating behaviors

The current-voltage curves of the films and substrates were detected by the four-probe method. The scanning voltages of Ti and Au-Ti samples were from −0.06 to 0.06 V, and the scanning voltages of MgFeO-Ti and Au/MgFeO-Ti samples were from −6 to 6 V. In addition, the samples were immersed in 1 ml of saline, and the localized proton concentration on the sample surfaces was detected using a pH microelectrode (InLab Micro, Mettler Toledo) for immersion times of 1, 2, 5, 10, 20, 40, and 60 min (three replicates for each group). A PL spectrometer (F-4600 FL) was used to detect the fluorescence emission spectra of the films on various samples, and the excitation light wavelength is 310 nm. AFM was used to detect the surface potential of the MgFe-MMO and Au/MgFe-MMO films.

Antibacterial performance evaluation

Gram-positive *S. aureus* (ATCC25923) and Gram-negative *E. coli* (ATCC25922) were selected to evaluate the antibacterial properties of various samples. *S. aureus* and *E. coli* were cultured with NB and LB media, respectively. Forty microliters of bacterial suspension at a density [10^7 colony-forming units (CFU)/ml] was inoculated on the sample surfaces and incubated in an incubator at 37°C.

After incubation for 12 hours, the antibacterial performances of various samples were detected by smear plate method. Briefly, the bacterial suspension on various sample surfaces was collected by shaking, and diluted 10^5 times with saline solution. One hundred microliters of the diluted bacterial suspension was evenly coated on the agar plate and cultured for 18 hours. Then, the agar plate was photographed and counted, and the corresponding antibacterial rate was calculated according to the following formula: $C = 100\% \times (A - B) / A$, where C represents the antibacterial rate; A represents the number of bacterial colonies of Ti group; and B represents the number of bacterial colonies of Ti, Au-Ti, MgFeO-Ti, and Au/MgFeO-Ti (three replicates for each group). Besides, bacteria on the samples were stained using a LIVE/DEAD BacLight kit (L13152) and were observed by fluorescence microscopy (GX71, Olympus, Japan). For bacterial morphology and structure observation, the bacteria were fixed by 2.5% glutaraldehyde for 4 hours and subsequently dehydrated and dried by graded concentrations of water/ethanol and ethanol/hexamethyldisilazane solutions, and the bacterial morphology was observed by SEM (S3400, Hitachi, Japan) and TEM (FEI Talos L120C, Thermo Fisher Scientific, USA).

Bacterial composition detection

After incubation on various samples for 6 hours, the intracellular ROS contents of bacteria were detected using DCFH-DA fluorescent probe (three replicates for each group). Bacterial protein leakage in the supernatants on various samples was detected using a BCA protein kit (three replicates for each group). After lysis of bacteria on various samples, the bacterial intracellular ATP content and the total bacterial protein content were measured using the Enhanced ATP Assay Kit and the BCA Protein Assay Kit, respectively. The bacterial intracellular ATP levels were normalized to the total protein and were presented as nanomoles per microgram of total proteins (three replicates for each group). The alamarBlue reagent was used to detect the activity of the bacteria after 6 hours of incubation on the samples (three replicates for each group). The medium containing 10% alamarBlue was used to coculture with the bacteria, and after 2 hours, the fluorescence intensity of 590-nm emitted light stimulated by 560-nm excitation light of the medium was detected using an enzyme-labeling instrument (Cytation 5, BioTek), and the value of fluorescence intensity was positively correlated with the bacterial activity.

Exploration of proton transfer of *S. aureus*

Forty microliters of *S. aureus* at a concentration of 10^7 CFU/ml was inoculated on the sample surfaces in a 24-well plate and incubated at 37°C for 6 hours. The pH fluorescent probe BCECF-AM and DAPI were added to stain the bacterial intracellular proton concentration and DNA, respectively. A fluorescence microscope (GX71, Olympus, Japan) was used to observe the number and the intracellular pH level of bacteria on various samples. BCECF-AM is a fluorescent dye that can penetrate the cell membrane. BCECF-AM is nonfluorescent and can be hydrolyzed by the bacterial esterase enzyme to form BCECF, which is retained within the bacteria. That is, the stronger the green fluorescence of BCECF, the higher the intracellular pH of bacteria; the stronger the blue fluorescence of DAPI, the higher the number of bacteria. In addition, 500 μl of *S. aureus* suspension with a density of 10^7 CFU/ml was inoculated on the samples, and the local proton concentration of extracellular microenvironment of bacteria cultured on the sample surfaces for 0, 10, 30, and 60 min and 2, 4, and 6 hours was detected using a pH microelectrode (four replicates for each group).

Exploration of electron transfer of *S. aureus*

An electrochemical workstation was used to detect the LSV curves of the samples. The sample, calomel electrode, and platinum electrode were used as work, reference, and counter electrodes, respectively. The voltage scanning range was from −0.5 to 0.2 V. To further investigate the electron transfer effect between bacteria and samples, *S. aureus* (10^8 CFU/ml) was inoculated on various samples and incubated for 10 min, and then the LSV curves of the samples in the presence of bacteria were subsequently measured using an electrochemical workstation. In addition, the CTC reagent was used to detect the concentration of electrons in the respiratory chain of the

bacterial membrane. Briefly, 40 μl of *S. aureus* at a concentration of 10^7 CFU/ml was inoculated on the sample surfaces and incubated for 6 hours at 37°C. The electron in the bacterial membrane was stained by adding CTC reagent. The CTC reagent could be reduced to CTC formazan by the bacterial membrane respiratory chain electrons, forming a water-insoluble and red-fluorescent precipitate inside the bacteria. Subsequently, DAPI reagent was used to stain the bacterial DNA. A fluorescence microscopy (GX71, Olympus, Japan) was used to observe the stained bacteria on various sample surfaces.

Transcriptomic analysis of *S. aureus*

S. aureus with a density of 10^8 CFU/ml was incubated on Ti and Au/MgFeO-Ti samples for 6 hours. Then, the bacterial precipitates were collected by centrifugation. Bacterial RNA was extracted using the RNAprep Pure Cell/Bacteria Kit. RNA sequencing was performed by NovaSeq 6000 (Illumina, CA, USA). Data analysis was done by Fastp (v0.23.1). GO (http://www.geneontology.org) and KEGG (http://www.genome.jp/kegg/) were used to analyze gene function. Differential gene expression analysis was performed using the R package DESeq2 (v1.20.0), and genes that met $|\log_2$ fold change$| > 0$ ($P < 0.05$) were considered differentially expressed genes (three replicates for each group).

In vitro cytocompatibility evaluation

The osteoblasts, fibroblasts, and macrophage (MC3T3-E1, L929, and RAW264.7) were used to evaluate the cytocompatibility of various samples. The cells were provided by the Cell Center of Shanghai Institutes for Life Sciences, Chinese Academy of Sciences. The MC3T3-E1 and L929 cells were cultured in an incubator (37°C and 5% CO_2) with α–minimum essential medium (Gibco, USA). MC3T3-E1 and L929 cells (2×10^4 cells per well) were inoculated on various samples for 1, 4, and 24 hours. Then, cells were fixed using 4% paraformaldehyde solution for 10 min. After permeabilizing the cells with 0.1% (v/v) Triton X-100, the nuclei and cytoskeleton were stained with DAPI and rhodamine, respectively, and the adhesion situation of cells on various samples was observed by fluorescence microscopy. The alamarBlue reagent was used to detect the proliferation rate of cells on the samples for 1, 4, and 7 days (three replicates for each group). Meanwhile, the cells cultured on the samples for 4 days were fixed using a 2.5% (v/v) glutaraldehyde solution, followed by dehydration and drying by graded concentrations of water/ethanol and ethanol/hexamethyldisilazane solutions. The bacterial morphology was observed by an SEM (S3400, Hitachi, Japan). Cells cultured on various samples for 4 days were stained using the cell live/dead staining kit, and the cells were observed using a fluorescence microscope. The mitochondrial membrane potential of the cells on the samples was stained using the JC-1 kit and was observed by fluorescence microscopy (BX63, Olympus, Japan).

In vivo biological performance assessment

Percutaneous infection model

All animal experiments in this study were approved by the Institutional Animal Care and Use Committee of Shanghai Rat & Mouse Biotech Co., Ltd (approval no. RM202301) (*15*). The 4- to 6-week-old C57BL/6J male mice were selected for the construction of a percutaneous implant infection model. Ti and Au/MgFeO-Ti rod samples with a diameter of 2 mm and a length of 20 mm were immersed in *S. aureus* suspension (1×10^7 CFU/ml) and incubated for 2 hours. The mice were randomly divided into two groups, and after anesthesia with 10% chloral hydrate, a wound through the skin was created on the back of the mice using a 2-mm-diameter Kirschner wire. Then, the rod samples with bacteria were implanted subcutaneously in the mice, and the ends of the rods were fixed with resin.

After 1 and 4 days of rearing, three mice in each group were randomly selected and euthanized using an overdose of anesthetic. The implants were removed from the backs of the mice, and the antibacterial effect of the implants was assessed by plate colony counting (three replicates for each group). The soft tissues surrounding the implants were collected, fixed, dehydrated, embedded, sectioned, and then observed under a light microscope after staining with Giemsa and H&E.

The mice were euthanized after 7 and 14 days of rearing, and the soft tissues around the implants were removed. The soft tissues were fixed, embedded, and sectioned, and then the sections were stained with Masson and VEGF. To evaluate the in vivo biosafety of the samples, mice were executed 14 days after implantation of the samples, and the heart, liver, spleen, lungs, kidneys, and other organs of the mice were removed for fixation, embedding, sectioning, and H&E staining, followed by observation using a light microscope.

Osteomyelitis model

The 8-week-old male Sprague-Dawley rats were selected and anesthetized using 4% chloral hydrate. After drilling holes with a diatom of 2 mm in the intercondylar area, the Ti and Au/MgFeO-Ti implant rods (2 mm in diameter and 8 mm in length) soaked with bacterial suspension were embedded into the holes individually, and the surgical area was subsequently sutured. After being reared for 1 week, the rats were euthanized by anesthetic overdose, and the implants were removed and placed in the NB medium for 16 hours. Then, the bacterial colony adhered to implant surfaces was evaluated using spread plate method. In addition, the femoral parts of the rats were collected, fixed, dehydrated, embedded, sectioned, and then stained with Giemsa and H&E before being observed using a light microscope.

After 6 weeks of rearing, the rats were euthanized by anesthesia overdose, and the femoral parts of the rats were collected and fixed with 4% paraformaldehyde. The new bone formation was detected using micro-CT after the samples were embedded in the femur of Sprague-Dawley rats, and the volume of new bone formed around the implanted samples was measured by a series of 3D reconstructions of 2D tomographic images (three replicates for each group). To evaluate the in vivo biosafety of the samples, mice were euthanized 6 weeks after implantation of the samples, and the heart, liver, spleen, lungs, kidneys, and other organs of the mice were removed for fixation, embedding, sectioning, and H&E staining, followed by observation using a light microscope.

Statistics analysis

The statistical analysis was carried out via GraphPad Prism Software, and the statistical significance of the difference (P) among groups was assessed using one-way/two-way analysis of variance (ANOVA). $P < 0.05$ was regarded as statistically significant. The symbols of *, **, and *** denote the P values of less than 0.05, 0.01, and 0.001, respectively.

Supplementary Materials

This PDF file includes:

Figs. S1 to S23

REFERENCES AND NOTES

1. C. R. Arciola, D. Campoccia, L. Montanaro, Implant infections: Adhesion, biofilm formation and immune evasion. *Nat. Rev. Microbiol.* **16**, 397–409 (2018).
2. W. Zimmerli, A. Trampuz, P. E. Ochsner, Current concepts: Prosthetic-joint infections. *N. Engl. J. Med.* **351**, 1645–1654 (2004).
3. B. H. Kapadia, R. A. Berg, J. A. Daley, J. Fritz, A. Bhave, M. A. Mont, Periprosthetic joint infection. *Lancet* **387**, 386–394 (2016).
4. N. D. Friedman, E. Temkin, Y. Carmeli, The negative impact of antibiotic resistance. *Clin. Microbiol. Infect.* **22**, 416–422 (2016).
5. R. O. Darouiche, Treatment of infections associated with surgical implants. *N. Engl. J. Med.* **350**, 1422–1429 (2004).
6. M. Godoy-Gallardo, U. Eckhard, L. M. Delgado, Y. J. D. de Roo Puente, M. Hoyos-Nogués, F. J. Gil, R. A. Perez, Antibacterial approaches in tissue engineering using metal ions and nanoparticles: From mechanisms to applications. *Bioact. Mater.* **6**, 4470–4490 (2021).
7. K. Huang, J. Wang, A. Zhuang, Q. Liu, F. Li, K. Yuan, Y. Yang, Y. Liu, H. Chang, Y. Liang, Y. Sun, X. Yan, T. Tang, P. J. Stang, S. Yang, Metallacage-based enhanced PDT strategy for bacterial elimination via inhibiting endogenous NO production. *Proc. Natl. Acad. Sci. U.S.A.* **120**, e2218973120 (2023).
8. D. P. Linklater, V. A. Baulin, S. Juodkazis, R. J. Crawford, P. Stoodley, E. P. Ivanova, Mechano-bactericidal actions of nanostructured surfaces. *Nat. Rev. Microbiol.* **19**, 8–22 (2021).
9. J. Jenkins, J. Mantell, C. Neal, A. Gholinia, P. Verkade, A. H. Nobbs, B. Su, Antibacterial effects of nanopillar surfaces are mediated by cell impedance, penetration and induction of oxidative stress. *Nat. Commun.* **11**, 1626 (2020).
10. Y. Zhang, J. Cui, K.-Y. Chen, S. H. Kuo, J. Sharma, R. Bhatta, Z. Liu, A. Ellis-Mohr, F. An, J. Li, Q. Chen, K. D. Foss, H. Wang, Y. Li, A. M. McCoy, G. W. Lau, Q. Cao, A smart coating with integrated physical antimicrobial and strain-mapping functionalities for orthopedic implants. *Sci. Adv.* **9**, eadg7397 (2023).
11. J. Huo, Q. Jia, H. Huang, J. Zhang, P. Li, X. Dong, W. Huang, Emerging photothermal-derived multimodal synergistic therapy in combating bacterial infections. *Chem. Soc. Rev.* **50**, 8762–8789 (2021).
12. S. Guan, S. Chen, X. Zhang, H. Zhang, X. Liu, Z. Hou, F. Wang, S. Qian, H. Zhu, J. Tan, X. Liu, Metastructure "trap" coating by acoustic confinement effect for antibacterial sonothermal therapy. *Adv. Funct. Mater.* **34**, 2316093 (2024).
13. B. Ran, L. Ran, Z. Wang, J. Liao, D. Li, K. Chen, W. Cai, J. Hou, X. Peng, Photocatalytic antimicrobials: Principles, design strategies, and applications. *Chem. Rev.* **123**, 12371–12430 (2023).
14. A. Y. Vargas-Lizarazo, M. A. Ali, N. A. Mazumder, G. M. Kohli, M. Zaborska, T. Sons, M. Garnett, I. M. Senanayake, B. M. Goodson, J. M. Vargas-Muniz, A. Pond, P. J. Jensik, M. E. Olson, S. D. Hamilton-Brehm, P. Kohli, Electrically polarized nanoscale surfaces generate reactive oxygenated and chlorinated species for deactivation of microorganisms. *Sci. Adv.* **10**, 5555 (2024).
15. J. Li, Y. Feng, W. Chen, S. Zhang, J. Ma, S. Chen, S. Liu, C. Cao, Y. Zhang, Electroactive materials: Innovative antibacterial platforms for biomedical applications. *Prog. Mater. Sci.* **132**, 101045 (2023).
16. I.-Y. Suh, Z.-Y. Huo, J.-H. Jung, D. Kang, D.-M. Lee, Y.-J. Kim, B. Kim, J. Jeon, P. Zhao, J. Shin, S. Kim, S.-W. Kim, Highly efficient microbial inactivation enabled by tunneling charges injected through two-dimensional electronics. *Sci. Adv.* **10**, 5067 (2024).
17. I. Vercellino, L. A. Sazanov, The assembly, regulation and function of the mitochondrial respiratory chain. *Nat. Rev. Mol. Cell Biol.* **23**, 141–161 (2022).
18. L. A. Sazanov, A giant molecular proton pump: Structure and mechanism of respiratory complex I. *Nat. Rev. Mol. Cell Biol.* **16**, 375–388 (2015).
19. Y. Z. Lai, Y. Y. Zhang, S. Zhou, J. X. Xu, Z. Q. Du, Z. Y. Feng, L. Yu, Z. Q. Zhao, W. W. Wang, Y. T. Tang, X. A. Yang, L. W. Guddat, F. J. Liu, Y. Gao, Z. H. Rao, H. R. Gong, Structure of the human ATP synthase. *Mol. Cell* **83**, 2137 (2023).
20. P. D. Boyer, The ATP synthase—A splendid molecular machine. *Annu. Rev. Biochem.* **66**, 717–749 (1997).
21. H. Guo, T. Suzuki, J. L. Rubinstein, Structure of a bacterial ATP synthase. *eLife* **8**, 43128 (2019).
22. J. G. Hurdle, A. J. O'Neill, I. Chopra, R. E. Lee, Targeting bacterial membrane function: An underexploited mechanism for treating persistent infections. *Nat. Rev. Microbiol.* **9**, 62–75 (2011).
23. H. Yang, A short review on heterojunction photocatalysts: Carrier transfer behavior and photocatalytic mechanisms. *Mater. Res. Bull.* **142**, 111406 (2021).
24. Y. Chen, Z. Wang, S. Chen, H. Ren, L. Wang, G. Zhang, Y. Lu, J. Jiang, C. Zou, Y. Luo, Non-catalytic hydrogenation of VO_2 in acid solution. *Nat. Commun.* **9**, 818 (2018).
25. W. Chen, A. Chen, X. Liu, F. Shu, J. Zeng, J. Zhang, H. Xu, G. Peng, Z. Yang, J. Li, G. Liu, Customization of 2D atomic-molecular heterojunction with manipulatable charge-transfer and band structure. *Adv. Mater.* **36**, 2410097 (2024).
26. J. Fu, W. Zhu, X. Liu, C. Liang, Y. Zheng, Z. Li, Y. Liang, D. Zheng, S. Zhu, Z. Cui, S. Wu, Self-activating anti-infection implant. *Nat. Commun.* **12**, 6907 (2021).
27. Q. Zhu, S. Jiang, K. Ye, W. Hu, J. Zhang, X. Niu, Y. Lin, S. Chen, L. Song, Q. Zhang, J. Jiang, Y. Luo, Hydrogen-doping-induced metal-like ultrahigh free-carrier concentration in metal-oxide material for giant and tunable plasmon resonance. *Adv. Mater.* **32**, 2004059 (2020).
28. G. Wang, K. Tang, Z. Meng, P. Liu, S. Mo, B. Mehrjou, H. Wang, X. Liu, Z. Wu, P. K. Chu, A quantitative bacteria monitoring and killing platform based on electron transfer from bacteria to a semiconductor. *Adv. Mater.* **32**, 2003616 (2020).
29. L. Wu, Y. Luo, C. Wang, S. Wu, Y. Zheng, Z. Li, Z. Cui, Y. Liang, S. Zhu, J. Shen, X. Liu, Self-driven electron transfer biomimetic enzymatic catalysis of bismuth-doped PCN-222 MOF for rapid therapy of bacteria-infected wounds. *ACS Nano* **17**, 1448–1463 (2023).
30. J. Li, W. Liu, D. Kilian, X. Zhang, M. Gelinsky, P. K. Chu, Bioinspired interface design modulates pathogen and immunocyte responses in biomaterial-centered infection combination therapy. *Mater. Horiz.* **6**, 1271–1282 (2019).
31. Y. Yu, Y. Zeng, Q. Ouyang, X. Liu, Y. Zheng, S. Wu, L. Tan, Ultrasound-induced abiotic and biotic interfacial electron transfer for efficient treatment of bacterial infection. *ACS Nano* **17**, 21018–21029 (2023).
32. S. Chen, F. Liu, H. Xin, D. Wen, Y. Zhang, B. Li, Y. Han, Boosting MRSA infectious osteoporosis treatment: Mg-doped nanofilm on vacancy-enriched TiO_2 coating for providing in situ sonodynamic bacteria-killing and osteogenic alkaline microenvironment. *Adv. Funct. Mater.* **34**, 2311965 (2024).
33. T. Ding, Y. Li, F. Liu, J. Chen, Y. Chen, L. Kong, Y. Han, L. Zhang, Electron spin polarization engineering in ferromagnetic bioheterojunction for sonotherapy of osteomyelitis. *Adv. Funct. Mater.* **34**, 2401795 (2024).
34. D. Zhang, J. Tan, R. Xu, H. Du, J. Xie, F. Peng, X. Liu, Collaborative design of MgO/FeO_x nanosheets on titanium: Combining therapy with regeneration. *Small* **19**, 2204852 (2023).
35. J. Wang, B. Hao, K. Xue, H. Fu, M. Xiao, Y. Zhang, L. Shi, C. Zhu, A smart photothermal nanosystem with an intrinsic temperature-control mechanism for thermostatic treatment of bacterial infections. *Adv. Mater.* **34**, 2205653 (2022).
36. H. Du, D. Zhang, F. Peng, K. W. K. Yeung, X. Liu, Two-dimensional layered double hydroxides for biomedical applications: From nano-systems to surface- and body-systems. *Prog. Mater. Sci.* **142**, 101220 (2024).
37. T. Hu, Z. Gu, G. R. Williams, M. Strimaite, J. Zha, Z. Zhou, X. Zhang, C. Tan, R. Liang, Layered double hydroxide-based nanomaterials for biomedical applications. *Chem. Soc. Rev.* **51**, 6126–6176 (2022).
38. J. Tan, D. Wang, H. Cao, Y. Qiao, H. Zhu, X. Liu, Effect of local alkaline microenvironment on the behaviors of bacteria and osteogenic cells. *ACS Appl. Mater. Interfaces* **10**, 42018–42029 (2018).
39. Q. Li, D. Wang, J. Qiu, F. Peng, X. Liu, Regulating the local pH level of titanium *via* Mg-Fe layered double hydroxides films for enhanced osteogenesis. *Biomater. Sci.* **6**, 1227–1237 (2018).
40. H. Fu, L. Wang, Q. Bao, D. Ni, P. Hu, J. Shi, Acid neutralization and immune regulation by calcium-aluminum-layered double hydroxide for osteoporosis reversion. *J. Am. Chem. Soc.* **144**, 8987–8999 (2022).
41. M. P. Casaletto, A. Longo, A. Martorana, A. Prestianni, A. M. Venezia, XPS study of supported gold catalysts: The role of Au^0 and $Au^{+\delta}$ species as active sites. *Surf. Interface Anal.* **38**, 215–218 (2006).
42. G. Wang, Y. Ling, D. A. Wheeler, K. E. N. George, K. Horsley, C. Heske, J. Z. Zhang, Y. Li, Facile synthesis of highly photoactive α-Fe_2O_3-based films for water oxidation. *Nano Lett.* **11**, 3503–3509 (2011).
43. X. Lu, Z. Ma, Y. Chang, S. Wang, X. Li, D. Xu, J. Bao, Y. Liu, Mott–Schottky construction boosted plasmon thermal and electronic effects on the Ag/CoV-LDH nanohybrids for highly-efficient water oxidation. *Adv. Mater.* **36**, 2313057 (2024).
44. P. P. Navarro, A. Vettiger, V. Y. Ananda, P. M. Llopis, C. Allolio, T. G. Bernhardt, L. H. Chao, Cell wall synthesis and remodelling dynamics determine division site architecture and cell shape in *Escherichia coli*. *Nat. Microbiol.* **7**, 1621–1634 (2022).
45. H. Wei, Y. Luo, C. Wang, S. Wu, Y. Zheng, Y. Zhang, J. Shen, X. Liu, Metal-organic framework-derived homologous sulfide heterojunction for robust enzyme-like self-driven bacteria-killing through enhanced electron transfer. *Small Methods* **7**, 2201618 (2023).
46. J. Tan, Z. Liu, D. Wang, X. Zhang, S. Qian, X. Liu, A facile and universal strategy to endow implant materials with antibacterial ability via alkalinity disturbing bacterial respiration. *Biomater. Sci.* **8**, 1815–1829 (2020).
47. J. Li, J. Wang, D. Wang, G. Guo, K. W. K. Yeung, X. Zhang, X. Liu, Band gap engineering of titania film through cobalt regulation for oxidative damage of bacterial respiration and viability. *ACS Appl. Mater. Interfaces* **9**, 27475–27490 (2017).
48. J. Li, H. Zhou, S. Qian, Z. Liu, J. Feng, P. Jin, X. Liu, Plasmonic gold nanoparticles modified titania nanotubes for antibacterial application. *Appl. Phys. Lett.* **104**, 261110 (2014).
49. M. Holeček, Branched-chain amino acids in health and disease: Metabolism, alterations in blood plasma, and as supplements. *Nutr. Metab.* **15**, 33 (2018).
50. D. Shore, B. Albert, Ribosome biogenesis and the cellular energy economy. *Curr. Biol.* **32**, R611–R617 (2022).

51. B. Ezraty, A. Gennaris, F. Barras, J.-F. Collet, Oxidative stress, protein damage and repair in bacteria. *Nat. Rev. Microbiol.* **15**, 385–396 (2017).
52. X. Huang, J. Xing, Z. Wang, J. Han, R. Wang, C. Li, C. Xiao, F. Lu, J. Zhai, Z. Zhou, Y. Li, L. Zhou, Z. Song, D. Chen, P. Yu, C. Ning, X. Jiang, 0D/1D heterojunction implant with electro-mechanobiological coupling cues promotes osteogenesis. *Adv. Funct. Mater.* **31**, 2106249 (2021).
53. X. Ma, Y. Zhou, M. Xin, H. Yuan, D. Chao, F. Liu, X. Jia, P. Sun, C. Wang, G. Lu, G. Wallace, A Mg battery-integrated bioelectronic patch provides efficient electrochemical stimulations for wound healing. *Adv. Mater.* **36**, 2410205 (2024).
54. P. Mitchell, Coupling of phosphorylation to electron and hydrogen transfer by a chemi-osmotic type of mechanism. *Nature* **191**, 144–148 (1961).
55. I. Belevich, M. I. Verkhovsky, M. Wikström, Proton-coupled electron transfer drives the proton pump of cytochrome *c* oxidase. *Nature* **440**, 829–832 (2006).
56. D. Wang, J. Tan, H. Zhu, Y. Mei, X. Liu, Biomedical implants with charge-transfer monitoring and regulating abilities. *Adv. Sci.* **8**, 2004393 (2021).

Acknowledgments: We thank X. Cao for help with the AFM (Bruker BNSM) test and R. Ding for help with the Raman and electrical test. **Funding:** This work was supported by the "Pioneer" and "Leading Goose" R&D Program of Zhejiang (2024C03080 to X.L.), the National Natural Science Foundation of China (52450110 to X.L. and 52293382 to J.N.), Science and Technology Commission of Shanghai Municipality (24ZR1475600 to J.T.), Beijing Municipal Health Commission (BMHC-2021-6 and BJRITO-RDP-2024 to D.C.), and Beijing Municipal Public Welfare Development and Reform Pilot Project for Medical Research Institutes (JYY2023-11 and JYY2023-8 to D.C.). **Author contributions:** Conceptualization: J.T. and X.L. Writing—original draft: J.T. Investigation: J.T. Visualization: J.T. Writing—review and editing: J.T., H.Z., Y.L., and X.L. Methodology: J.T., H.Z., Y.L., Z.H., D.W., J.Z., B.Z., Y.Cui, S.Q., Y.D., K.H., J.N., and S.Y. Project administration: J.T. Data curation: J.T. and H.Z. Software: J.T. and Y.Cao. Formal analysis: J.T. and H.Z. Supervision: X.L. and J.T. Resources: X.L. and D.C. Funding acquisition: X.L., D.C., and J.T. **Competing interests:** The authors declare that they have no competing interests. **Data and materials availability:** All data needed to evaluate the conclusions in the paper are present in the paper and/or the Supplementary Materials.

Submitted 30 October 2024
Accepted 19 February 2025
Published 19 March 2025
10.1126/sciadv.adt3159